Journal of Power Sources 476 (2020) 228593

Contents lists available at ScienceDirect

Journal of Power Sources

journal homepage: www.elsevier.com/locate/jpowsour

Perspective

Towards high-performance Li-ion batteries via optimized three-dimensional micro-lattice electrode architectures

Yaqi Zhu [a], Jie Li [a], M. Sadeq Saleh [b], Hiep Pham [a], Tazdik Patwary Plateau [a], Rahul Panat [b,**], Jonghyun Park [a,*]

[a] Department of Mechanical and Aerospace Engineering, Missouri University of Science and Technology Rolla, Missouri, 65401, USA
[b] Department of Mechanical Engineering, Carnegie Mellon University, Pittsburgh, PA, 15213, USA

HIGHLIGHTS

- Identify the ionic and electronic transport in additively fabricated 3D electrodes.
- Macro/micro mechanical responses of 3D electrodes during charging/discharging.
- Correlate battery performance with shapes, thicknesses, packing density, porosities.
- Optimize the length scale of members forming electrode structures.
- 3D electrode designs and manufacturing routes for superior battery performance.

GRAPHICAL ABSTRACT

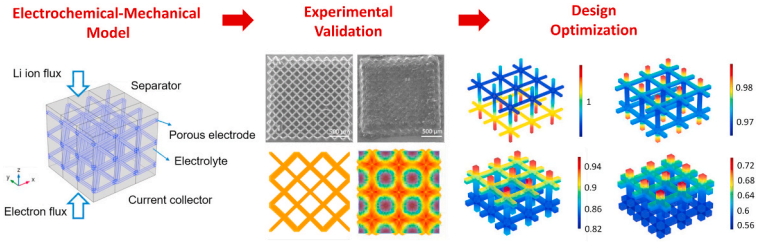

ARTICLE INFO

Keywords:
Microstructure
3D electrodes
Aerosol jet printing
Charge transport
Macro/micro deformation
Stress analysis

ABSTRACT

Optimized three-dimensional (3D) electrode architectures hold the promise of improving battery performance, a goal that cannot be obtained via conventional laminated structures. This paper reports on the mechanisms by which 3D electrodes enhance battery performance. The diffusion/migration of electrons/ions inside the battery was comprehensively analyzed via a 3D electrochemical model and subsequently validated by experiments on 3D micro-lattice electrodes made by Aerosol Jet printing. Lithium concentration and potential distribution were mapped to correlate battery performance with different shapes, thicknesses, packing density, and porosities. The study revealed that the main factors determining battery performance are ion diffusion in the electrolyte and electron transport in the 3D electrode skeleton. Further, the emergence of a competition between available volume for intercalation and an easier electronic/ionic path was shown, which determined their areal/specific capacities. In order to fully reap the benefits offered by 3D structures for both energy and power performance, the length scale of members forming electrode structures needs to be optimized at a scale of the order of the intercalation diffusion length, which is tens of micrometers. This study reveals highly useful guidelines for optimized 3D electrode designs and the possible manufacturing routes to realize them in order to achieve superior battery performance.

* Corresponding author.
** Corresponding author.
E-mail addresses: rpanat@andrew.cmu.edu (R. Panat), parkjonghy@mst.edu (J. Park).

https://doi.org/10.1016/j.jpowsour.2020.228593
Received 24 January 2020; Received in revised form 7 June 2020; Accepted 24 June 2020
Available online 18 August 2020
0378-7753/

1. Introduction

Lithium ion batteries are one of the most important energy storage systems for portable devices, transportation, and renewable grids. To meet the increasing requirements by these applications, batteries with a higher energy and power density are urgently needed. Battery performance can be improved either by using higher capacity electrode materials or by improving the transport of the species during battery operations. Although significant progress has been made in these areas, most of the materials used in today's commercial Li-ion batteries are similar to those discovered about 20–30 years ago [1,2]. A different route to increase battery capacity and power is to create well-defined, three-dimensional (3D) porosity within the electrodes [3–6]. For example, conventional laminated composite electrodes fabricated via a tape casting process show a trade-off between energy density and power density. To improve the energy density, more active material needs to be loaded by increasing the electrode thickness and packing density. This, however, limits the transport of ions and electrons, leading to poor power performance and inefficient utilization of the electrode materials. A 3D lattice electrode structure, on the other hand, allows an increase in surface-to-volume ratio, enabling the electrolyte to penetrate through the electrode volume. The free surface also reduces lithiation stress, enabling the use of high-capacity materials that undergo large volumetric changes during the battery's electrochemical cycles. Lastly, 3D-structured electrodes enable large specific surface area and short ion diffusion lengths which in turn enhance the energy density without much sacrifice of power density.

The manufacture of 3D-structured electrodes at microscales has been challenging because of the fact that most microfabrication methods have been largely planar. Recent advances in 3D printing (i.e., additive manufacturing), however, have opened new pathways to realize geometrically optimized electrode architectures. The first 3D micro-battery was fabricated in an interdigitated structure with $Li_4Ti_5O_{12}$ (LTO) and $LiFePO_4$ (LFP) by an extrusion-based direct ink writing technique. The micro-battery showed a high areal energy density of 9.7 J/cm^2 with a power density of 2.7 mW/cm^2 [7]. Subsequently, electrode performance was enhanced by interdigitated structures of graphene oxide-based $LiFePO_4$ and $Li_4Ti_5O_{12}$ [8], $LiMn_{0.21}Fe_{0.79}PO_4$ [3], $LiMnO_4$ [9], reduced chemically-modified graphene (rCMG) [10], and CNF-based LFP/Li [11]. In addition, multilayered thick electrodes of different patterns, such as the grid [12] and Z patterns [13,14], were developed. However, the use of interdigitated structures is limited in the further improvement of porosity and pore volume because of their simple geometry, which plays an important role in the electron transport and mechanical stress relief [15]. Other methods to create 3D-architected electrodes include self-assembled nanolattices of an electrolytically active material sandwiched between rapid ion and electron transport pathways that exhibit high charge-discharge rates [16,17]. Si-electrodes with porosities at a length scale of >20 μm were shown to relieve strain and prevent pulverization of the anodes during electrochemical cycling [18]. Lastly, hollow gold tube electrodes, fabricated with periodic pores with sizes in the hundreds of nanometers using two-photon lithography followed by atomic layer deposition, were used in Li-ion batteries for fundamental electrochemical studies [19,20].

Recently, complex 3D micro-lattice electrodes with a hierarchical porosity over several orders of magnitude in length scale were reported to be achieved by Aerosol Jet (AJ) 3D printing [21]. AJ is an innovative, noncontact printing process that deposits aerosolized microdroplets of nanoparticles dispersed in a solvent onto a substrate to create 3D structures such as lattices [22]. Compared with traditional extrusion and inkjet printing, the AJ method facilitates the use of a large viscosity range for inks (up to 1000 cP) and a stand-off height of up to 5 mm between the substrate and nozzle, which enables printing on complex 3D substrates [23,24]. The length scale of the truss members of the lattice structure is about 10 μm [21], a scale comparable to the characteristic diffusion length of Li ions in several host materials for reasonable charge-discharge times. Further, the sintering process creates an internal porosity within the truss members, which is of the order of a micron or less, thus forming a hierarchical porous structure [21].

For energy storage devices, a hierarchical electrode porosity in three dimensions provides several advantages [25–28]. For example, the electrochemical performance of the electrode material would be influenced not only by submicron scale porosity via parameters such as pore size, pore distribution, and pore morphology, but also by macroscale porosity that forms the electrode structure. During the AJ 3D printing process, the submicron scale porosity can be adjusted by sintering parameters and the macroscale electrode structure is determined by the initial design/printing program [22]. Theoretically, pores can facilitate the species transport from the electrolyte to the electrode surface. However, too small pores would impede species movement. On the other hand, volumetric energy density is reduced by the existence of large pores [29]. The macro-porous Sn–Cu alloy electrode has an average pore size of 180 nm, and it delivered a reversible capacity of 350 mAh/g in the 70th cycle, improving on the 270 mAh/g attributed to an average pore size of 500 nm [30]. In 3D-ordered macro-porous $Li_4Ti_5O_{12}$ electrodes, a porous internal wall structures exhibited better rate capability and extremely high capacities [31]. In mesoporous anatase TiO_2, the specific capacities of electrodes increased as the pore size of the surfactants used in the preparation increased from 5.7 nm to 7.0 nm [32]. The interconnectivity between pores is also critical for electrode performance because it affects the electrolyte distribution. For example, in mesoporous anatase TiO_2 a uniform pore size distribution was reported to be beneficial because it allowed an optimal open volume for best mass transport without wasted space [28]. In a study of 3D vanadium pentoxide aerogel, the tortuosity of the material was reduced by a hierarchically-ordered, inverted opal structure, leading to less polarization and a high capacity at high C-rate compared with bulk aerogels [33]. In addition, pore structure was shown to correlate with both surface area and pore wall thickness of the electrode material [34,35]. Large specific surface area can effectively reduce the current density per unit surface area, alleviating the polarization at the interface and facilitating ion transfer [36]. Further, pore wall thickness determines the length of lithium ion diffusion during the intercalation and deintercalation process, impacting the capacity and rate capability of the material [37,38]. It is notable that few studies have reported an experimental realization of electrodes with feature sizes of the order of 10s of micrometers [21,39,40]. Our previous work on Aerosol Jet printed electrodes [21] showed a significant improvement in areal capacity for X-structure compared to block structures of Ag electrodes (100% increase with electrode thickness increasing from 200 μm to 450 μm). A near-complete utilization of the electrode volume for micro-lattice scaffolds was also observed. Extrusion-based additive manufacturing [39] was used to fabricate 3D electrodes with feature sizes of tens of micrometers that exhibited improved electrochemical performance. Chemical etching was used to fabricate 'sponge-like' Si structures with feature sizes in tens of micrometers that showed a significant improvement in battery capacity with minimal capacity fade [40].

Although it has been shown that 3D-structured electrodes can improve battery performance, the extra freedom related to geometrical construction and its complex influence on electrochemical properties necessitates better understanding of the mechanisms of performance enhancement to allow the identification of optimized 3D electrode structures. Because it is too costly to use experimental trial and error methods, numerical modeling, validated by experiments for a few geometries, provides an effective way to predict the electrochemical properties of different sets of parameters while reducing time and cost. Over the past decades, several studies have been performed to include the features of electrode structure in battery performance simulations. For example, tortuosity was regarded as a key parameter to represent the impact of geometry on battery properties [41]. It was implemented as a correction factor for effective material properties such as mass transport, liquid phase diffusivity, and conductivity. Tomography was utilized as a

way to input the microstructural information of the electrodes [15,42]. The microstructure of electrodes can be meshed according to X-ray nano-CT images or SEM images [42] by using the finite volume method, thus allowing for the investigation of the spatial distribution of electrochemical properties in the model. Some works also implemented a 3D finite element scheme based on assumptions on particle size selection, arrangement, and material properties [43,44]. In these works, microstructure was created by assembling particles in random or pre-set arrays in a unit cell with periodic boundary conditions. However, all the models mentioned above consider microstructural information only at the micro-scale while assuming a homogenous structure at the macro-scale. To take into account the effect of both micro- and macro-scale pores in 3D electrode architectures, a model that is able to separately consider structural information at different scales needs to be developed.

Mechanical deformation and failure of the electrodes are important factors affecting battery electrochemical performance. The intercalation and de-intercalation of Li ions can cause an expansion and contraction of electrode volume, leading to micro and/or macro-scale stress generation in the electrode [45,46]. This chemically induced stress is even more important for electrodes with 3D complex shapes, and can affect their mechanical stability during the charge-discharge cycles [21]. In addition, possible structural defects in such electrodes can amplify the stresses, adversely affecting their cyclic life and capacity [45,47]. This effect can be studied by introducing an electromechanical-mechanical coupling term in the battery models. In few past studies, the impact of stress generation, particle deformation, crack propagation, and diffusion have been investigated in a single particle [48–52]. Several researchers also report macro-scale models that account for geometrical changes such as thickness increase and thermal swelling [53–56]. None of these studies [48–56], however, considered complex 3D electrode architectures in their models.

In this paper, we analyze the effect of macro- and microscale structural features of 3D lattice-shaped electrodes on battery performance using a 3D electrochemical-mechanical model. In this model, the micro-scale structures are implemented based on a porous electrode theory, while the macro-scale structures are modeled by a 3D finite element scheme. The model is validated by experimental observation based on AJ printed 3D micro-lattice electrode Li-ion battery cells. The impact of two-level structural porosity on the electrochemical properties of the battery is analyzed by including different volume fractions of the solid phase at the micro-scale and different electrode geometries and their electrode thicknesses at the macro-scale. This extensive study on the relationship between micro/macro electrode geometry and battery performance provides the scientific basis to facilitate high-capacity electrode designs that can be realized by additive manufacturing.

2. Experimental setup

A 40 ± 2 wt % Ag nanoparticle ink with a particle size of 30–50 nm and a viscosity of 1.5 cP (Perfect-TPS 50 G2, Clariant Group, Frankfurt, Germany) was adopted for printing. The ink was loaded into a commercial AJ printer (AJ-300, Optomec, Inc. Albuquerque, NM) to be deposited in a 3D geometry on a chromium-coated stainless steel connector disk of 11 mm diameter and 500 μm thickness under ambient conditions. The geometry of the electrode was drawn in AutoCAD by the software AutoLISP (AutoCAD 2015, Autodesk Inc. San Rafael, CA) and imported into the printer controller to guide the printing process. Subsequently, the printed pattern was sintered at 350 °C for 2 h in a programmable oven (Neytech Vulcan furnace, Model 3–550, Degussa-Ney Dental Inc. Bloomfield, CT). The detailed preparation process of the 3D electrodes was presented in our previous paper [21].

A CR2032 coin cell (Wellcos Corp) was used to assemble a battery in an argon-filled glove box (Mbraun). A printed silver lattice was used as the working electrode (theoretical specific capacity 290 mAh/g). The counter electrode, separator, and electrolyte were Li foil (Sigma Aldrich), commercial PP/PE/PP membrane (Celgard), and 1 M $LiFP_6$ EC: DMC 1:1 v/v (Sigma-Aldrich), respectively. The charge/discharge process was conducted from 0.02 to 2.8 V using a battery test station (IVIUMnSTAT, Ivium Tech).

3. Electrochemical model

A 3D full-order electrochemical model was developed and implemented to evaluate the performance of the 3D lattice electrodes. The model is based on the porous electrode theory [57], where an electrode sketch is incorporated in the geometry and meshed by the finite element method. The Li ion concentration in the solid phase was evaluated via a fourth-order approximate analytic solution of the solid-phase diffusion equation [58]. Pore structure and then 3D geometry of the electrode that form the two-level porosity were treated as being at different scales: the pore structure was regarded as a homogenized system superimposed by electrode and electrolyte and the 3D geometry was simulated as if it were composed of individual solid and liquid phases [44]. To incorporate the 3D geometry of the electrode into the model, a half-cell model was developed as shown in Fig. 1. The mass conservation and charge conservation equations were evaluated in a 3D electrode according to the porous electrode theory, shown in Fig. 1b. The equations used in the 3D model are summarized in Table 1. COMSOL 5.4 was used to implement all governing equations above into finite element simulation to determine the electrochemical behavior within the 3D electrodes schematized in Fig. 1b. The material parameters used in the simulation are listed in Table 2.

4. Results and discussion

4.1. Model validation using experimental results

4.1.1. Voltage profile

Schematics of the 3D electrodes' lattice structure used for model validation along with a unit cell are shown in Fig. 1c. Two electrode structures fabricated by AJ printing – an open octahedral structure (called 'X-structure' in this paper) and a solid block-structure – are shown in Fig. 1d. In the X-structure, the diameter of the electrode truss members of the micro-lattice was about 35 μm, which is on the same order of magnitude as the characteristic diffusion length ($\sqrt{Dt}$) for full lithiation at 0.5 C. The pore size in the printed micro-lattice structure was about 100 μm × 100 μm, which is sufficient for the electrolyte (viscosity <10 cP) to undergo capillary absorption [59]. The truss members of the electrode had an internal porosity ranging between 500 nm–1 μm, also described in our previous work [21]. The block electrode and the X-structured electrode exhibited similar thicknesses of approx. 450 μm.

Fig. 1e shows a comparison between the measured discharge profiles of the two types of electrodes and the model prediction, respectively. The model predictions for both X-structure and block-electrode geometry show good agreement with the experimental data, which indicates that the modeling approach developed in this work can be used to capture the effect of electrode geometry on battery performance. The spatial distributions of state-of-charge (SOC) in the X- and the block structure are plotted in Fig. 1f. When the capacity of a structure is larger, its SOC distribution is expected to be more uniform, and the average SOC is expected to be closer to 1, that is, a fully charged state. Note that the top surface in the Z-axis is the electrode/separator interface and the bottom side is the electrode/collector interface. For the block structure, a limitation in species transport results in a maximum SOC of 0.54 along with a high concentration gradient from the electrode/separator interface to the electrode/current collector interface (ΔSOC being 0.32). This leads to a small average SOC for the entire electrode. By contrast, the SOC in the open octahedral structured electrode is larger than 0.99 at all positions, indicating a high utilization of the electrode material. This

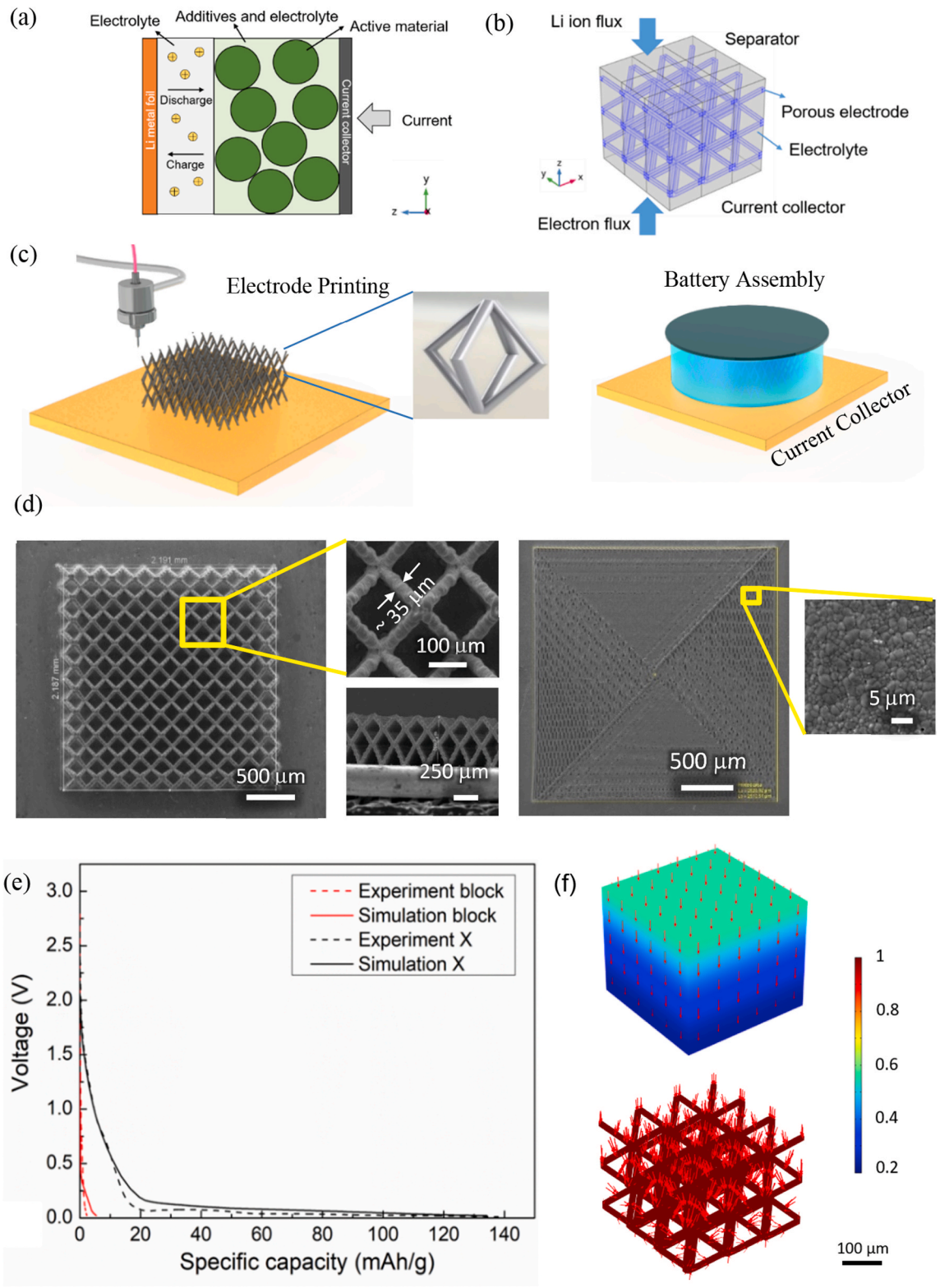

Fig. 1. Half-cell and model description: (a) Illustration of half-cell with porous electrode, (b) 3 × 3 × 3 array of 3- dimensional open octahedral micro-lattice structure (called "X-structure") used to develop the electrochemical model; 3D micro-lattice battery electrode experiments and model validation. (c) Schematic of aerosol jet (AJ) printing process to fabricate 3D micro-lattice structures, along with a schematic of the battery assembly process, (d) AJ-printed open octahedral electrode architecture (called 'X-structure' in this paper, left) and block electrode architecture (right). **Model validation:** (e) Comparison of battery performance for 3D printed electrodes with the model developed in the work demonstrating good agreement. (f) Spatial SOC distribution and flux distribution (red arrows) at 0.02 V for the open octahedral electrodes and block-structured electrodes. SEM image and simulated deformation of (g) X-structure electrode and (h) block-structure electrode in (left) as-fabricated state (0% capacity, x = 0) and (center) fully lithiated state (100% capacity, x = 1). Stress distribution of fully lithiated state in X-structure electrode (i) and block-structure electrode (j). Morphology evolution (k) at 20%, 40%, 60% and 80% capacity (x = 0.2, 0.4, 0.6 and 0.8). (For interpretation of the references to colour in this figure legend, the reader is referred to the Web version of this article.)

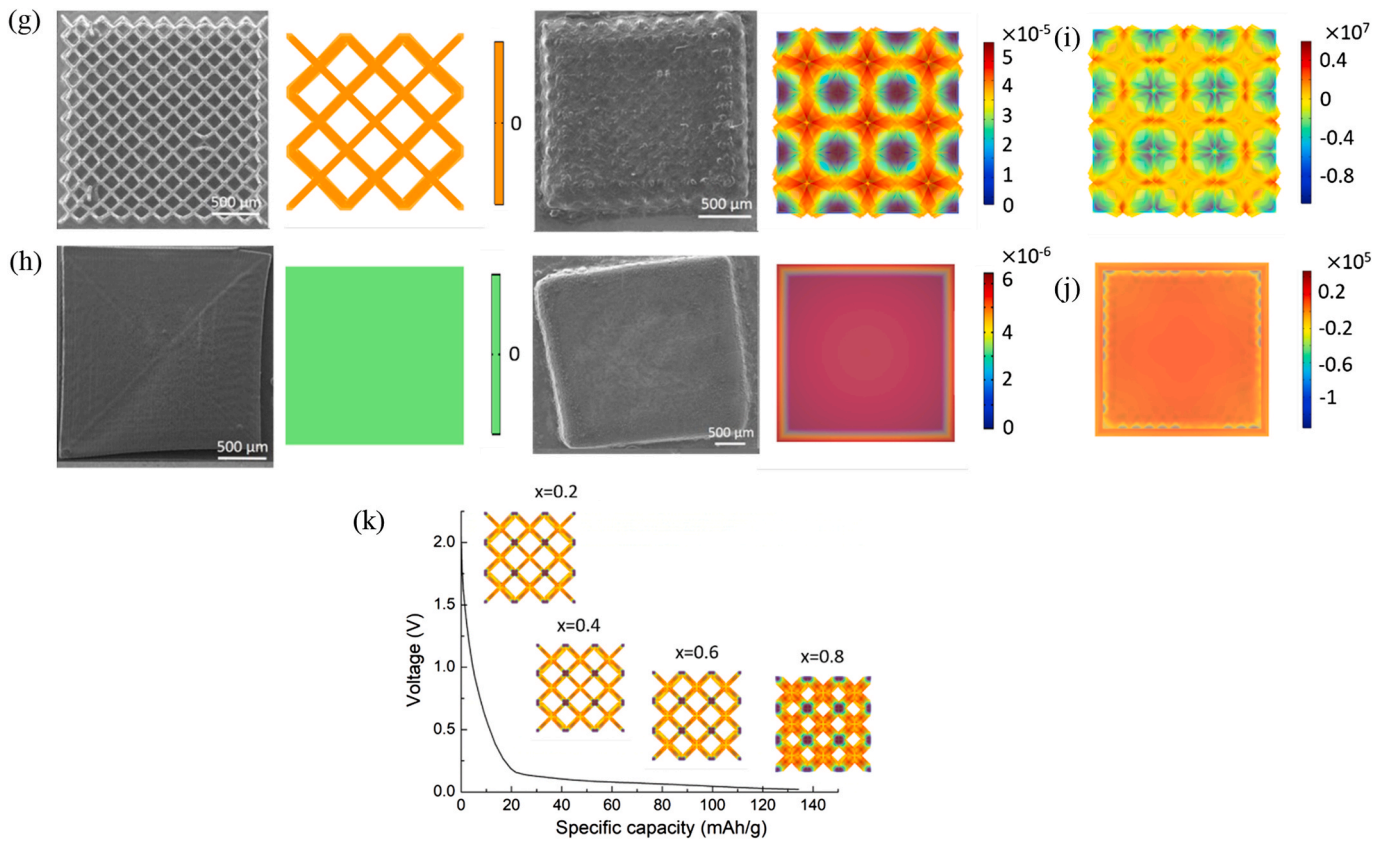

Fig. 1. (*continued*).

significantly improved behavior was attributed to the geometry of the 3D electrodes, which enhances the transport of the lithium ions. As indicated by the red arrows (representing flux), lithium ion flux was able to distribute at the surface of every unit lattice of the octahedral structure in various directions, rather than entering the electrode material only from the top surface in the block structure, which greatly improved the efficiency of lithium ion transfer.

4.1.2. Li-ion intercalation induced electrode displacement

It was observed in the experiments that the morphology of X-structured electrodes changed considerably after intercalation with Li-ions (Fig. 1g and h), which was caused by the volume change induced by the variation in the Li-ion concentration. To simulate this phenomenon, a stress model was developed by coupling the electrochemical-mechanical interaction at macro- and micro-scales. We note that since the battery model developed in this work is based on the porous theory, the mechanical response of the electrode should be interpreted based on a multiscale perspective. The micro-scale stress model deals with the stress generated inside the particle induced by Li ion concentration change. The macro-scale stress model deals with the stress generated across the entire skeleton caused by the volume change of individual particles. In the micro-scale, the particles were assumed as spheres. Therefore, the radial stress, σ_r, and tangential stress, σ_t, of individual particle can be expressed as [49].

$$\sigma_r = \frac{2\Omega E}{3(1-\upsilon)}\left(\frac{1}{r_0^3}\int_0^{r_0} c_{s,avg} r^2 dr - \frac{1}{r^3}\int_0^{r} c_{s,avg} r^2 dr\right) \tag{13}$$

$$\sigma_t = \frac{\Omega E}{3(1-\upsilon)}\left(\frac{2}{r_0^3}\int_0^{r_0} c_{s,avg} r^2 dr + \frac{1}{r^3}\int_0^{r} c_{s,avg} r^2 dr - c_{s,avg}\right) \tag{14}$$

where r_0 is the radius of the particle, E is the effective Young's modulus, υ is Poisson ratio, and Ω is the partial molar volume expansion of silver which is obtained from first-principles simulations and fitting of experimental data. The simulation data of $AgLi_x$ volume expansion and derivative process of Ω from a density functional theory (DFT) calculation are shown in Supplementary Material.

At particle surface ($r = r_0$)

$$\sigma_r = 0 \quad \sigma_t = \frac{\Omega E}{3(1-\upsilon)}\left(c_{s,avg} - c_{s,surf}\right) \tag{15}$$

The tangential stress-strain relations and strain-displacement relations can be expressed as

$$\varepsilon_t = \frac{1}{E}(\sigma_t - \upsilon(\sigma_r + \sigma_t)) + \frac{\Omega}{3}c_{s,avg} \tag{16}$$

$$\varepsilon_t = \frac{u}{r} \tag{17}$$

By importing Eq. (15) into Eq. (16) and Eq. (17), the particle surface displacement can be obtained as

$$u_{surf} = \frac{\Omega r_0}{3}\left(c_{s,avg} - c_0\right) \tag{18}$$

In spherical particles, the micro-scale chemically induced eigenstrain $\boldsymbol{e}_s^{ch}$ is equal to the particles' volumetric strain, which is

$$\boldsymbol{e}_s^{ch} = \frac{1}{3}\left(\frac{\left(r_0 + u_{surf}\right)^3}{r_0^3} - 1\right) \tag{19}$$

According to the Mori-Tanaka effective-field theory, the particle surface pressure is decided by the macro-scale total strain and the micro-scale volumetric strain. Therefore, the macro-scale eigenstrain $\boldsymbol{e}^{ch}$ can be computed as [56].

$$\boldsymbol{e}^{ch} = \boldsymbol{e}_m^{ch} + \varepsilon_s\left(\boldsymbol{e}_s^{ch} - \boldsymbol{e}_m^{ch}\right) + \varepsilon_s\left(\boldsymbol{C}_s^{-1} - \boldsymbol{C}_m^{-1}\right)b_s \tag{20}$$

Table 1
Governing equations in 3D model.

Region	Governing Equation	Boundary conditions
Electrode	**Mass, solid phase** $\frac{dc_{s,p,avg}(\mathbf{X},t)}{dt} = -\frac{J_p(\mathbf{X},t)}{3R_p}$ (1)	$c_{s,p,surf}(\mathbf{X},t) = c_{s,p,avg}(\mathbf{X},t) + \frac{8R_p}{35} q_{s,p,avg}(\mathbf{X},t) - \frac{R_p}{35D_{s,p}} J_p(\mathbf{X},t)$ (3)
	$\frac{dq_{s,p,avg}(\mathbf{X},t)}{dt} = -30\frac{D_{s,p}}{R_p^2} q_{s,p,avg}(\mathbf{X},t) - \frac{45}{2R_p^2} J_p(\mathbf{X},t)$ (2)	
	Charge, solid phase $\sigma_{eff,p} \nabla\varphi_{s,p}(\mathbf{X},t) = a_p F J_p(\mathbf{X},t)$ (4)	Current collector/anode interface: $-\sigma_{eff,p}\left(\frac{\partial\varphi_{s,p}(t)}{\partial x} + \frac{\partial\varphi_{s,p}(t)}{\partial y} + \frac{\partial\varphi_{s,p}(t)}{\partial z}\right)\Big\|_{z=0} = I_{app}$ (5)
Electrode/Separator	**Mass, liquid phase** $\varepsilon_j \frac{\partial c_{e,j}(\mathbf{X},t)}{\partial t} = \frac{\partial}{\partial \mathbf{X}}\left(D_{eff,j}\frac{\partial c_{e,j}(\mathbf{X},t)}{\partial \mathbf{X}}\right) + a_j(1-t_+)J_j(\mathbf{X},t)$ (6)	Separator/anode interface: $-D_{eff,s}\frac{\partial c_{e,s}(t)}{\partial \mathbf{X}}\Big\|_{z=l_p+l_s} = \frac{J_{Li}(t)}{F}$ (7)
	Charge, liquid phase $\kappa_{eff,j}\nabla^2\varphi_{e,j}(\mathbf{X},t) - \frac{2\kappa_{eff,j}RT(1-t_+)\partial^2 \ln c_{e,j}(\mathbf{X},t)}{F\partial \mathbf{X}^2}\left(1+\frac{d\ln f_+}{d\ln c_{e,j}}\right) = J_j(\mathbf{X},t)$ (8)	Separator/anode interface: $\kappa_{eff,j}\nabla\frac{\partial\varphi_{e,j}(\mathbf{X},t)}{\partial \mathbf{X}} - \frac{2\kappa_{eff,j}RT(1-t_+)\partial \ln c_{e,j}(\mathbf{X},t)}{F\partial \mathbf{X}}\left(1+\frac{d\ln f_+}{d\ln c_{e,j}}\right)\Big\|_{z=l_p+l_s} = J_{Li}(t)$ (9)
Electrode kinetics	$J_p\left(\mathbf{X},t\right) = k_p c_{s,p,\max}^{0.5}\left(1-\frac{c_{s,p,surf}(\mathbf{X},t)}{c_{s,p,\max}}\right)^{0.5}\left(\frac{c_{s,p,surf}(\mathbf{X},t)}{c_{s,p,\max}}\right)^{0.5}\left(\exp\left(\frac{0.5F}{RT}\eta_p(\mathbf{X},t\right)\right) - \exp\left(-\frac{0.5F}{RT}\eta_p(\mathbf{X},t\right)\right)\right)$ (10)	
	$\eta_p = \varphi_{s,p} - \varphi_{e,p} - U_p$ (11)	
	$J_{Li}(t) = 0.85\left(\exp\left(-\frac{0.5F}{RT}\varphi_{e,s}(\mathbf{X},t)\right) - \exp\left(\frac{0.5F}{RT}\varphi_{e,s}(\mathbf{X},t)\right)\right)$ (12)	

Table 2
Model parameters used in simulation studies.

Parameter	Value	Description
brug [44]	1.5	Bruggeman coefficient
$C_{e,k,0}$ [44]	2000	Initial electrolyte concentration (mol m^{-3})
$C_{\max,\ pos}$	102870	Maximum concentration of Li-ion in cathode (mol m^{-3})
D_e [44]	7.5×10^{-11}	Diffusion coefficient in electrolyte ($m^2 s^{-1}$)
$D_{s,p}$ [44]	2.5×10^{-15}	Solid-phase Li diffusivity, positive electrode ($m^2 s^{-1}$)
F	96487	Faraday's constant (C mol^{-1})
i_0 [44]	0.85	Constant flux for half-cell
I	Variable	Applied current density (A m^{-2})
$K_{s,p}$ [44]	3.8	Solid phase conductivity (S m^{-1})
k_p [44]	2×10^{-6}	Reaction rate coefficient, cathode ($m^{2.5} mol^{-0.5} s^{-1}$)
R	8.314	Universal gas constant (J mol^{-1} K^{-1})
R_p [44]	13×10^{-6}	Particle radius, positive electrode (m)
t_+ [44]	0.363	Cationic transport number
ε_p	Variable	Solid phase volume fraction of cathode
ε_s [44]	0	Solid phase volume fraction of separator
E	2.82×10^6	Effective Young's module (Pa)
ν	0.37	Poisson's ratio
Ω	1.15×10^{-4}	Partial molar volume expansion of Ag ~ AgLi (m^3 mol^{-1})
	6.07×10^{-6}	Partial molar volume expansion of AgLi ~ $AgLi_{1.8}$ (m^3 mol^{-1})

where ε_s is solid phase volume fraction, and $\boldsymbol{e}_m^{ch}$ is the chemically induced strain in the electrolyte, which is assumed to be 0 here. $\boldsymbol{C}_s$ and $\boldsymbol{C}_m$ are the stiffness matrices for the solid and liquid phase; while b_s is a function of $\boldsymbol{C}_s$ and $\boldsymbol{C}_m$.

The governing equation of macro-scale mechanical deformation is

$$\nabla \cdot \boldsymbol{\sigma} = 0 \tag{21}$$

$$\boldsymbol{\sigma} = \boldsymbol{C}_{eff} : (\boldsymbol{e} - \boldsymbol{e}_{ch}) \qquad e = \frac{1}{2}\left(\nabla \boldsymbol{u} + \nabla \boldsymbol{u}^T\right) \tag{22}$$

where $\boldsymbol{\sigma}$ is the macro-scale stress, $\boldsymbol{e}$ is the total macro-scale strain tensor and $\boldsymbol{u}$ is the total displacement, $\boldsymbol{C}_{eff}$is the effective elasticity tensor can be calculated as

$$\boldsymbol{C}_{eff} = \boldsymbol{C}_m + \varepsilon_s(\boldsymbol{C}_s - \boldsymbol{C}_m)\boldsymbol{A}_s \tag{23}$$

$$\boldsymbol{A}_s = \boldsymbol{A}_D\left[(1-\varepsilon_s)\boldsymbol{I} + \varepsilon_s \boldsymbol{A}_D\right]^{-1} \tag{24}$$

$$\boldsymbol{A}_D = \left[\boldsymbol{I} + \boldsymbol{S}\boldsymbol{C}_m^{-1}(\boldsymbol{C}_s - \boldsymbol{C}_m)\right]^{-1} \tag{25}$$

$\boldsymbol{S}$ is Eshelby's tensor, which is a function of the aspect ratio of the particle and the Poison's ratio of the matrix phase.

A comparison of simulated deformation of the X-structured and block-structured electrodes with the experimental observations is shown in Fig. 1g and h, respectively. For the X-structure, when the electrode was fully lithiated, the deformation resulted in complete filling of the spaces between truss members and the maximum displacement of the electrodes was located at the crosslinks, which matches quite well with the experiments (SEM images in Fig. 1g). For the block structure, the electrode shape did not change upon lithiation. This was because the SOC change in the block structure was not as large as that in the X structure as shown previously in Fig. 1f, and, according to Eq. (15), the volume expansion was proportional to SOC changes. This result also matches with the experimental observations (SEM images in Fig. 1h). The corresponding spatial distributions of stress are shown in Fig. 1i and j. As shown, the maximal stress in X-structure was around 5.93 MPa in the centers of truss members, while the maximal stress in block was 87.9 kPa at the edges of sides. Although the stress levels of those two structures are much smaller than the yielding point of the order of 100 MPa, the stress level of block structure is smaller than in X-structure for two reasons. First, the SOC change from as-fabricated state to fully charged state in block structure is around 50% less than that in X-structure (Fig. 1f). Secondly, the partial molar volume for Ag ~ AgLi (0–55.56%

SOC) is less than that for AgLi ~ $AgLi_{1.8}$ (55.56%–100% SOC) according to the first-principles calculation and fitting of the experimental data (see section S2 of the Supplementary Material). Therefore, both the volume changes and stress in block structure is smaller than that of X-structure. The evolution of the X-structure as a function of SOC as predicted by our model is shown in Fig. 1k. The volume expansion increased with the increasing of capacity ratio (x) under intercalation of Li ions. It is noted that the volume change from $x = 0$ to $x = 0.6$ was not as large as that from $x = 0.6$ to $x = 1$ due to the nonuniform of the partial molar volume at different SOC range. The reason for this phenomenon is that the volume expansion does not scale linearly with x. The partial molar volume for Ag ~ AgLi is less than that for AgLi ~ $AgLi_{1.8}$ according to the first-principles calculation and fitting of the experimental data (see section S2 of the Supplementary Material). Therefore, the silver electrode has a larger volume expansion at high SOCs. The excellent match between the SEM images and simulation results for volume expansion are a good validation for 3D model developed in this work. Further, by coupling the stress part, this electrochemical-mechanical model can also be applied to analyze the mechanical stability of other 3D electrodes in the future.

4.2. Effect of micro-lattice geometry on battery performance

4.2.1. State of charge for different electrode geometries

First, to investigate the impact of microlattice structure on battery performance, three different 3D lattice architectures were considered because they can be fabricated by 3D printing techniques [21,60]. The schematics of the unit cells of these structures are shown in Fig. 2a. The first unit cell was formed by diagonally joining the corners of an octahedron without the horizontal elements; it was identified as the "X-structure" (same as the micro-lattice electrode in Fig. 1d). The second unit cell was constructed by solid square prisms perpendicular to each other in x, y, and z directions (i.e., "cubic-structure"). The third unit cell was constructed by subtracting a sphere from a solid cube (i.e., "inverse sphere-structure"). To exclude the influence of mass, the investigated structures were manipulated to be identical in mass in the same-sized box (330 μm × 330 μm × 305 μm). As shown in Fig. 2b and c, the specific capacities of the X-s and the cubic-structure at 0.5 C discharge capacity were similar (at approx. 190 mAh/g), while the specific capacity for the inverse sphere-structured electrode was lower (approx. 146 mAh/g). At a discharge current of 0.5 C and 0.8 C, the capacity of the cubic-structure was 1.8% and 2.2% higher than that of the X-structure, and the capacity of the inverse sphere-structure was 24.1% and 36.4% lower than that of the X-structure, respectively. This large difference in discharge capacity was attributed to the non-uniform distribution of lithium ions in these three structures, as shown in Fig. 2d. It can be seen that at 0.02 V, the ranges of SOC in both the X- and the cubic-structure were 0.7–0.9, with a low SOC gradient. In the inverse sphere-structure, the SOC range increased and reached 0.54–0.68 (max), indicating low efficiency in material utilization.

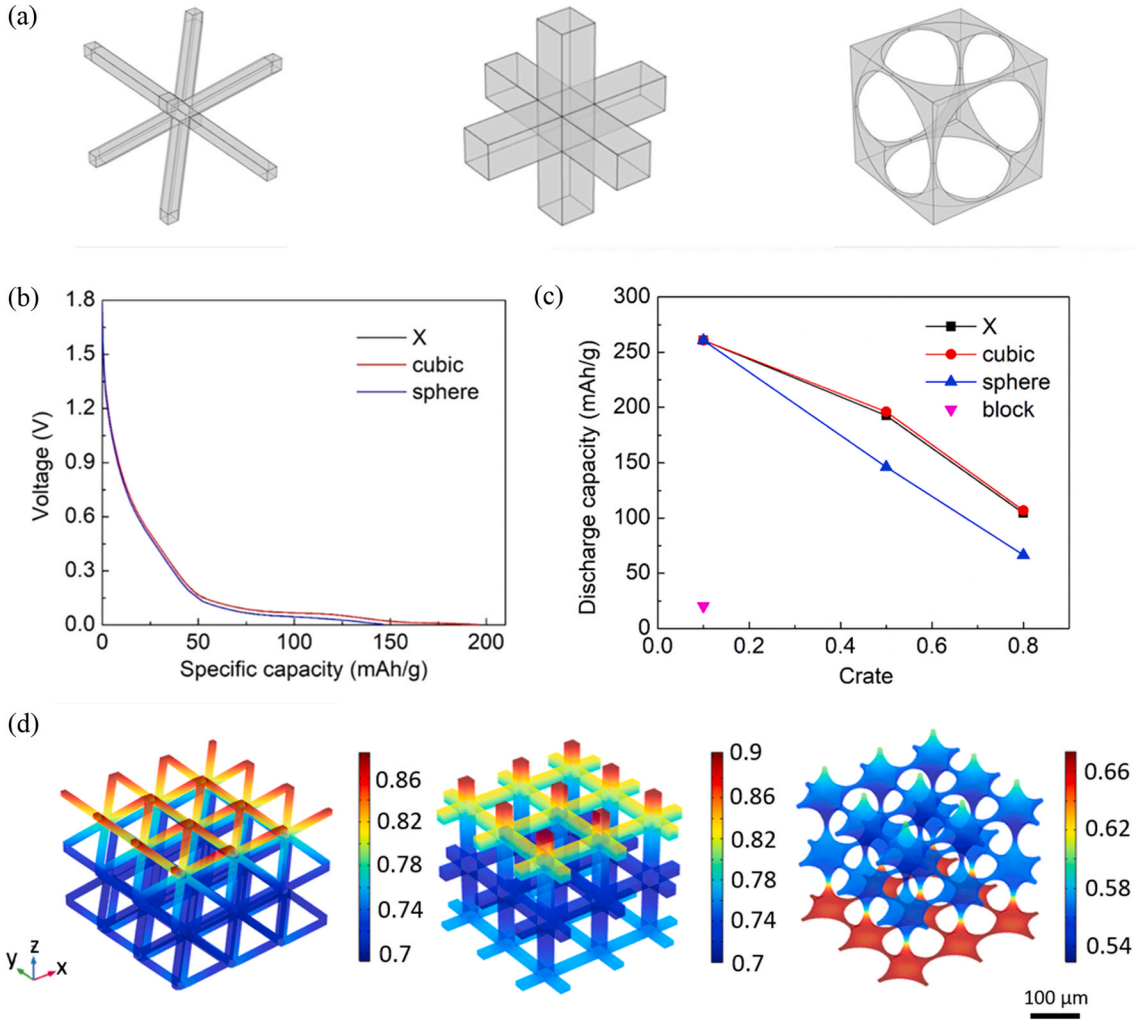

Fig. 2. Comparison between three different lattice structures. (a) Unit cell of X-structure (left), cubic-structure (center), and inverse sphere-structure (right), (b) discharge voltage profile at 0.5 C, (c) discharge capacity at 0.1 C, 0.5 C, and 0.8 C, (d) spatial SOC distribution at the end of discharge.

4.2.2. Impact of micro-lattice structures on species transport

In the X- and cubic-structure, SOC reaches its maximum value at the separator/electrode interface and then gradually decreases towards the electrode/collector interface. In case of the inverse sphere-structure, however, the maximal SOC is seen at the electrode/collector interface, which is opposite to conventional laminated structures where the current is generally higher at the separator side. The observed phenomenon was attributed to the changes in electron and ion transport as a function of electrode geometry. To shed further light on this phenomenon, the spatial and temporal distribution of the lithium concentration were analyzed. They are affected by many factors, including Li ion diffusion in solid and liquid phases and electron transport in the solid phase. For solid phase diffusion, it turns out that the lithium ion diffusion is not the limiting factor in determining battery performance. When the Li ion diffusivity (D) in the solid phase is increased by a factor of 10, the battery capacity remains almost the same as the original D ($D = 2.5 \times 10^{-15}$ m^2s^{-1}) (See Figs. S1 and S2). This indicates that Li ion diffusivity is relatively large and not a limiting factor in the diffusion processes. ***It is thus concluded that Li ion diffusion in the liquid phase and electron transport in the solid phase are the two primary factors affecting the electrochemical processes through the 3D lattice structures.*** As shown in Fig. 1b, electron transport occurs from the current collector side to the separator side of the electrode so that the solid phase potential gradually increases from bottom to top. Meanwhile, Li ions diffuse from the

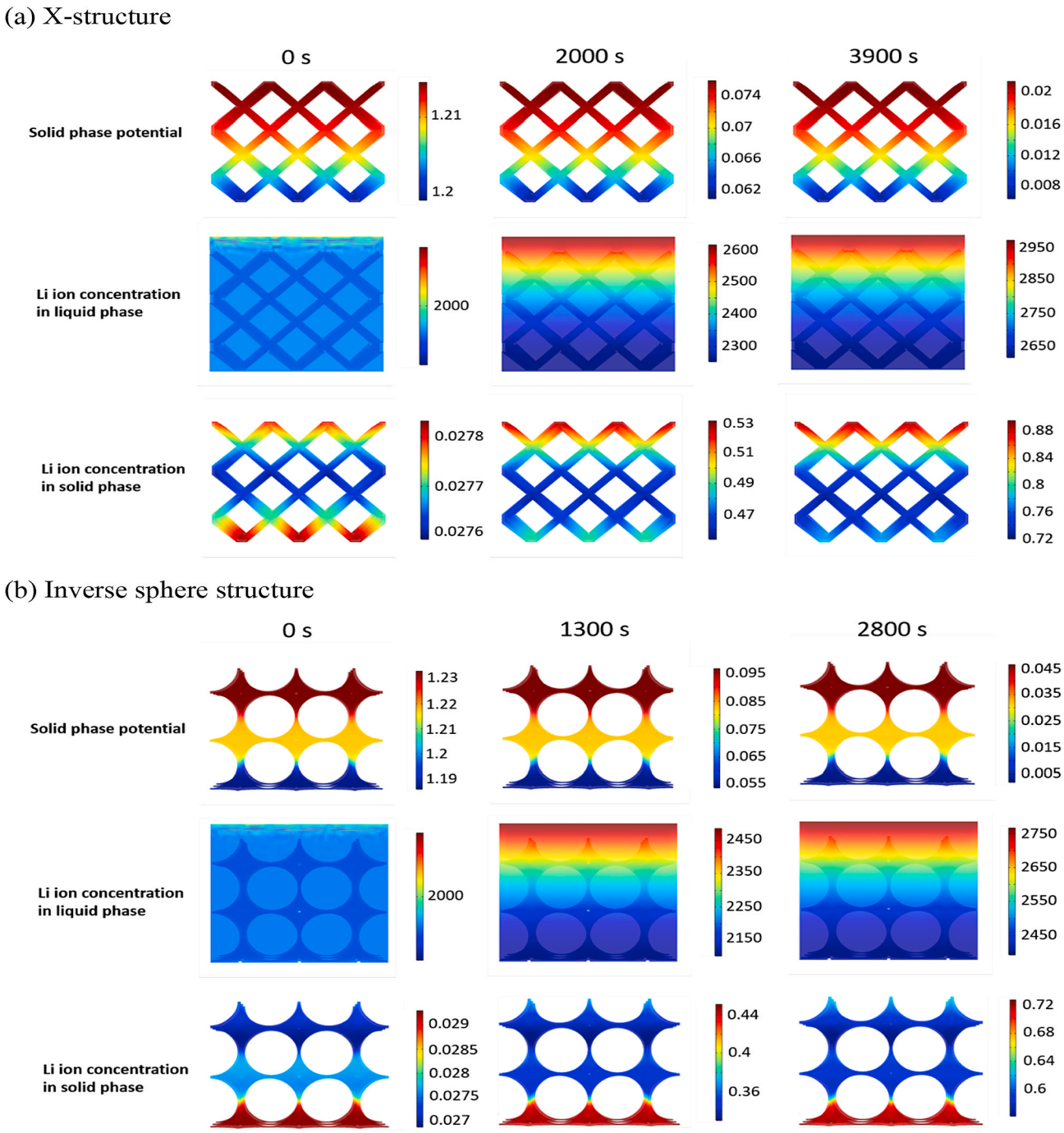

Fig. 3. Temporal distribution of solid phase potential, Li ion concentration in the liquid phase and solid phase. (a) X-structure at 0 s, 2000 s, and 3900 s, and (b) inverse sphere-structure at 0 s, 1300 s, and 2800 s; **Effect of geometry** (c) The distribution of the gradient of solid phase potential in Z direction (V/m) at the end of the discharge process, (d) p_s^{eff} and q_s^{eff}, (e) p_2^{eff} and q_2^{eff} and (f) S_s of different structures.

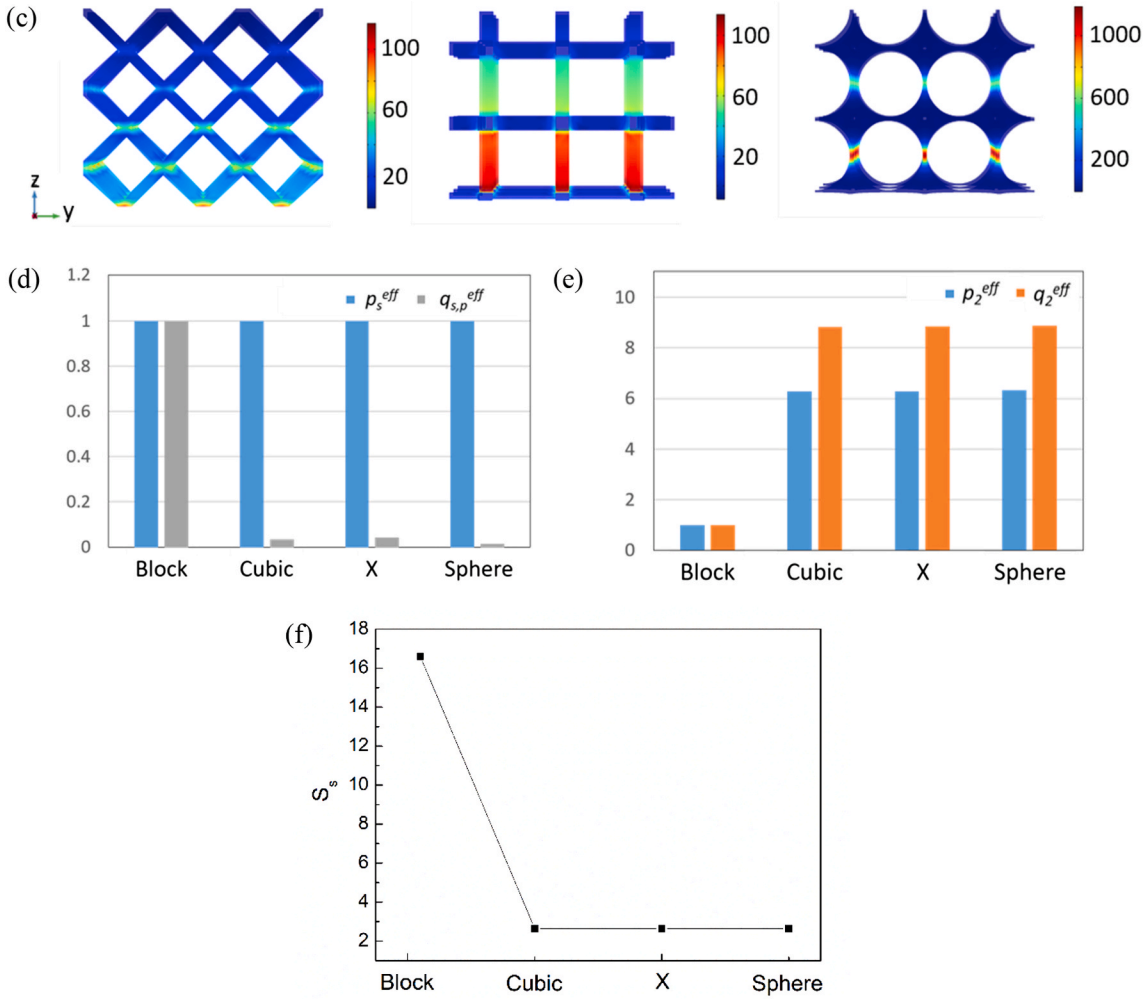

Fig. 3. (*continued*).

separator to cathode section, decreasing the electrolyte concentration from top to bottom. According to Eq. (10), the intercalation flux is affected by electrolyte concentration and electric potential, which eventually affect lithium distribution and SOC.

The temporal evolution of the spatial distribution of SOC, electrolyte concentration, and solid phase potential in X- and inverse sphere-structures are plotted in Fig. 3a and Fig. 3b, respectively. It can be seen that in the X-structure, at 0 s, both the electrolyte and solid phase potential gradients are very small (3.55 mol/L and 0.01 V), having a negligible impact on SOC distribution. Therefore, the maximal SOC is located at both the top and bottom side. However, the impact of electrolyte concentration becomes overwhelming as time evolves. As a result, the maximum SOC is distributed only at the top side at the end of the discharge. However, in the inverse sphere-structure (Fig. 3b), the difference of solid phase potential is larger than that in the X-structure (approx. 0.04 V from 0 s to 3900 s), while the electrolyte concentration gradient is almost the same for both. Therefore, the effect of the solid phase potential is dominant with respect to SOC distribution during the entire discharge process, and SOC is always maximal at the bottom. This significant potential gradient was attributed to the characteristic geometry of the electrodes. The comparison of potential gradients of the three structures is shown in Fig. 3c. It can be seen that crosslinks or bottlenecks in the structures, such as the intersection of hexagonal prisms in the X-structure, the cubic column in the *z*-direction in the cubic-structure, and the thinnest part at the column in the sphere-structure, often occupy a larger potential gradient because the electron transport is impeded. **The largest gradient of the solid phase potential in the sphere-structure is about 1000 V/m, which is nearly 10 times that of the gradient in the other two geometries, indicating a severe limitation in electron transport caused by the geometry.**

4.2.3. Mechanisms of electron and ion transport

To further understand the coupled physics of ion and electron transport in the solid and liquid phase, the individual transport phenomena were analyzed by decoupling them and obtaining the effective diffusivity for each. The diffusion and conduction in the solid and liquid were examined by the ratio of effective diffusion coefficient or conductivity to the material diffusion coefficient or conductivity, which are expressed as p_s^{eff}, q_s^{eff}, p_2^{eff}, q_2^{eff} and defined as:

$$p_s^{eff} = \frac{D_{s,p}^{eff}}{D_{s,p}}$$

$$q_s^{eff} = \frac{K_{s,p}^{eff}}{K_{s,p}}$$

$$p_2^{eff} = \frac{D_2^{eff}}{D_2}$$

$$q_2^{eff} = \frac{K_2^{eff}}{K_2} \tag{13}$$

in which $D_{s,p}^{eff}$ is the effective solid phase diffusion coefficient which is

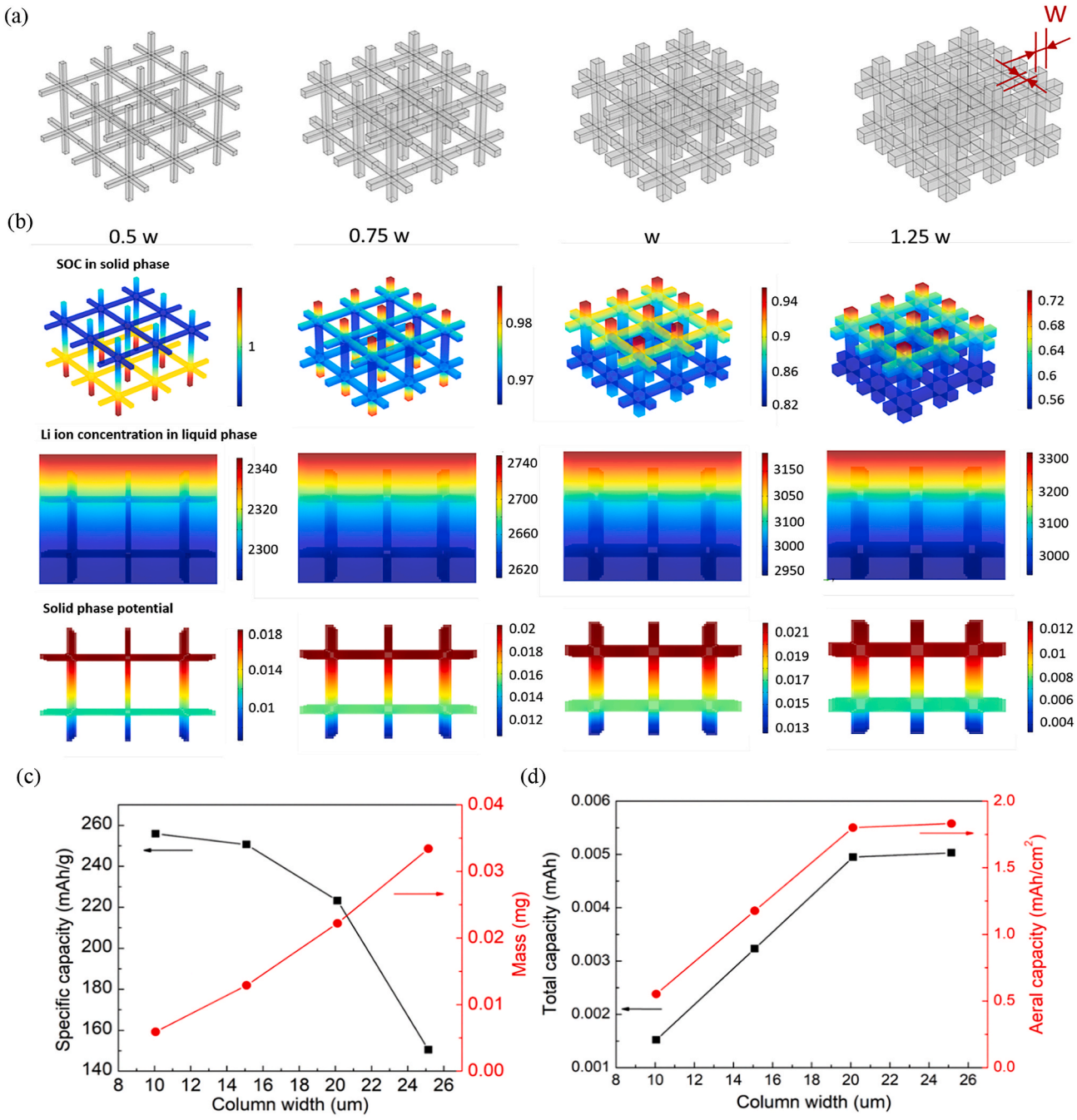

Fig. 4. Effect of column width in cubic structures (a) Schematics of different cubic structures with different column widths, (b) distribution of SOC, electrolyte concentration, and solid phase potential at the end of the discharge in cubic structures with different column width. (c, d) Specific capacity and total mass, and total capacity and areal capacity, (e, f, g) p_s^{eff}, q_s^{eff}, p_2^{eff}, q_2^{eff} and S_s, as functions of column width in the cubic structure.

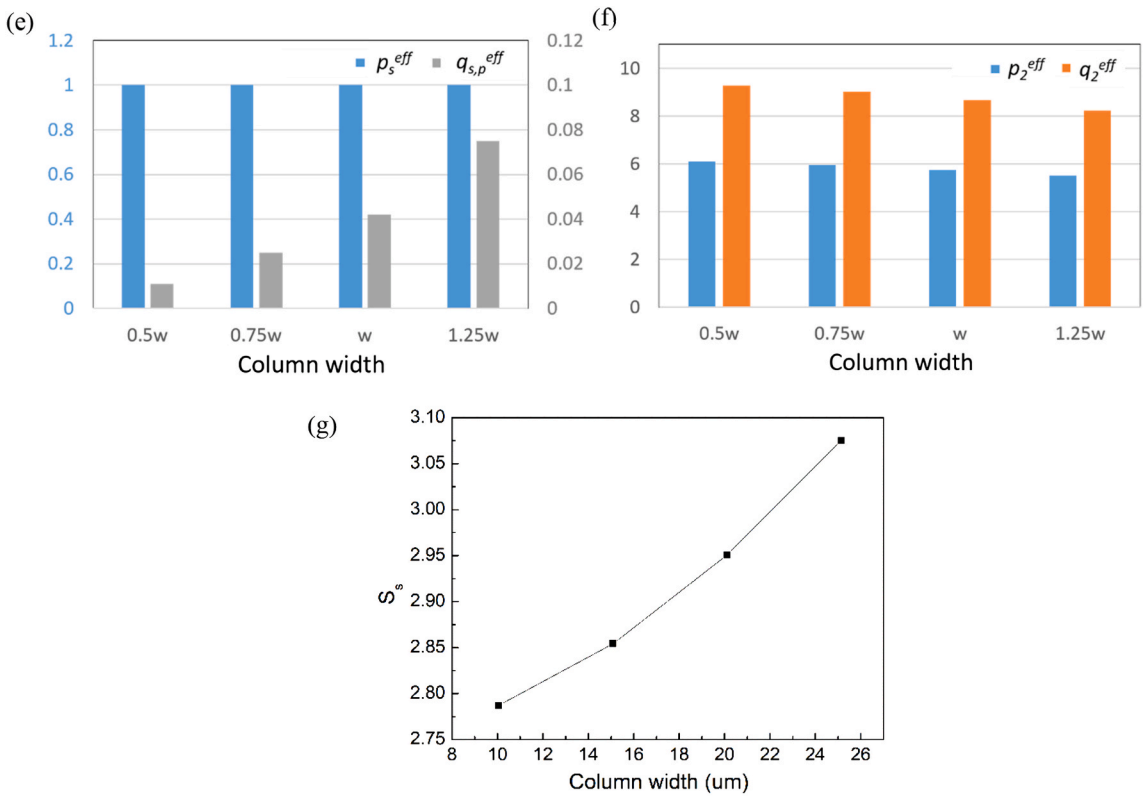

Fig. 4. (*continued*).

evaluated using an equivalent model of one particle. The surface Li ion concentration gradient in the one particle model is matched with that in 3D model. $K_{s,p}^{eff}$, D_2^{eff} and K_2^{eff} are the effective solid phase conductivity, effective liquid phase diffusion coefficient, and effective liquid phase conductivity, respectively, which were evaluated in a 1D model with corresponding individual physics of Li ion diffusion or electron transport. The final effective transport properties were obtained when the gradient of Li ion concentration was matched with that in a 3D model of the same physics. In particular, for the electrolyte, the relative characteristic times of electrolyte transport in relation to the discharge time, S_s, was analyzed further [47]:

$$S_s = \frac{(l_{sep} + l_{pos})^2 I}{D_2 p_2^{eff} F \varepsilon_p c_{\max,pos} l_{pos}} \tag{14}$$

where l_{sep} and l_{pos} are the thickness of separator and positive electrode, respectively. I is the applied current density, D_2 is the electrolyte diffusion coefficient, and p_2^{eff} is the ratio of effective diffusion coefficient to the electrolyte diffusion coefficient given above. Note that the solid phase diffusion time is not considered as it is not a limiting factor as explained earlier.

As shown in Fig. 3d and e, initially the values of p_s^{eff} exhibited almost no differences between different geometries, because $D_{s,p}^{eff}$ is mainly determined by the particle radius. If the flux is same, there is no critical difference inside single particles within an electrode. However, the values of $q_{s,p}^{eff}$ were 1, 0.035, 0.041, and 0.014 for block, cubic-, X-, and inverse sphere-structures respectively, indicating that 3D structures reduced electron transport in the solid phase compared with traditional laminated structures. This can be attributed to the reduction in solid phase by the 3D structures, leading to a reduction in path length for electron transport. In particular, the inverse-sphere structure showed a significant reduction, which can explain the phenomenon shown in Fig. 3b and c.

On the other hand, the values of p_2^{eff} and q_2^{eff} were very similar between all three 3D geometries. Both were much larger than those of the block structure, ***indicating that 3D structures are effective in improving the species transport in the liquid phase***. Unlike conduction in the solid phase, the removal of material to form a 3D structure enhanced the transport in the liquid phase. As a result, S_s decreased from 16 in block structures to ~2.5 in 3D structures, indicating significantly improved Li ion diffusion, which makes the Li diffusion as a less-limiting factor compared to the electron transport (Fig. 3f).

4.3. Optimized electrode designs

4.3.1. Cubic-structured electrodes

To obtain optimal electrode designs, we investigated the effect of different micro-lattice geometric parameters on the electrochemical performance of batteries. There are two factors determining the macro-scale porosity in the cubic structure: column width and distances between the columns. First, different column widths were investigated: 0.5 w, 0.75 w, 1 w, and 1.25 w ($w = 20.12$ μm) (Fig. 4a). As shown in Fig. 4b, as the column width increased, the SOC distribution became non-uniform and the electrode volume utilization decreased. Further investigation of the effect of column width on electrolyte concentration and solid phase potential showed that the concentration gradient of the electrolyte increased with a wider column. On the other hand, solid phase potential gradually decreased while the column width increased, see Fig. 4b. This was attributed to the positive effect of the wider column on electron transport (as shown in Fig. 4e). Overall it was determined that electron transport was a main limiting factor in the case of 0.5 w width, and that the electrolyte concentration contributed more with increasing column width to become dominant in the cases of 1 w and 1.25 w. Based on the above analysis, the increased areal flux is the primary reason for a more non-uniform distribution of SOC in cubic structures with wider columns compared to those with slender columns. As a result, the specific capacity decreased as the column width increased (Fig. 4c).

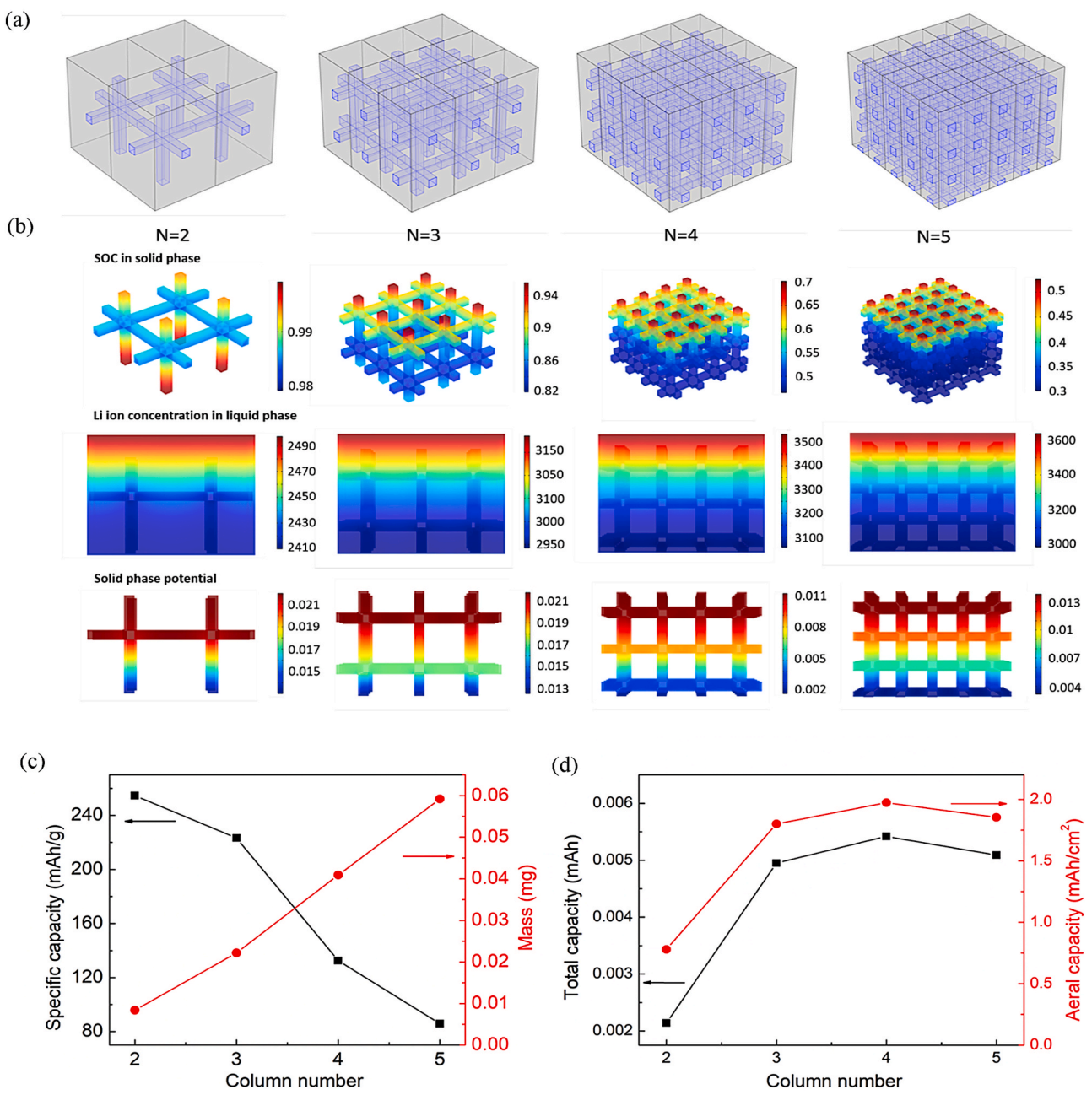

Fig. 5. Effect of number of columns in cubic structures. (a) Schematic of cubic structure with different numbers of columns, (b) distribution of SOC, electrolyte concentration, and solid phase potential at the end of the discharge in cubic structures with different numbers of columns. (c, d) Specific capacity, total mass, total capacity, and areal capacity, (e, f, g) p_s^{eff}, q_s^{eff}, p_2^{eff}, q_2^{eff}, and S_s as functions of number of columns in cubic structures.

Areal capacity is another key performance attribute that needs to be considered in electrode design, as it characterizes the electrode's energy density. Although specific capacity decreased with column width, the total mass of the electrode increased as a result of denser packing of active material, leading to increased total capacity. This increase, however, tapered off at widths wider than 20 μm as seen in Fig. 4d (note that the projected areas of the electrodes are identical). As the specific capacity and areal capacity exhibited a trade-off in this case, the optimal value of column width needs to be chosen according to the target property of the electrode design. The characteristic transport properties are also illustrated in Fig. 4e, f, and g. It is seen that the increase in column width enhanced electron transport in the solid phase. However, it also impeded species transport in the electrolyte (p_2^{eff} and q_2^{eff} decreased and S_s increased).

Next, the effect of the change in distance between columns in cubic structures on battery electrochemical performance was investigated. The column distance was manipulated by changing the number of columns in a unit cell from 2 to 5, as shown in Fig. 5a. It can be seen in Fig. 5b that the solid phase potential difference for all numbers of column were around 0.009 V, indicating that the change in the number of columns has little impact on electron transport. On the other hand, the electrolyte concentration gradient increased as the number of columns increased because of the increase in flux at the current collector/cathode interface. Consequently, the electrolyte concentration became determining as the number of columns in the unit cell increased from 3 to 5. Because of the larger electrolyte concentration gradient, the SOC

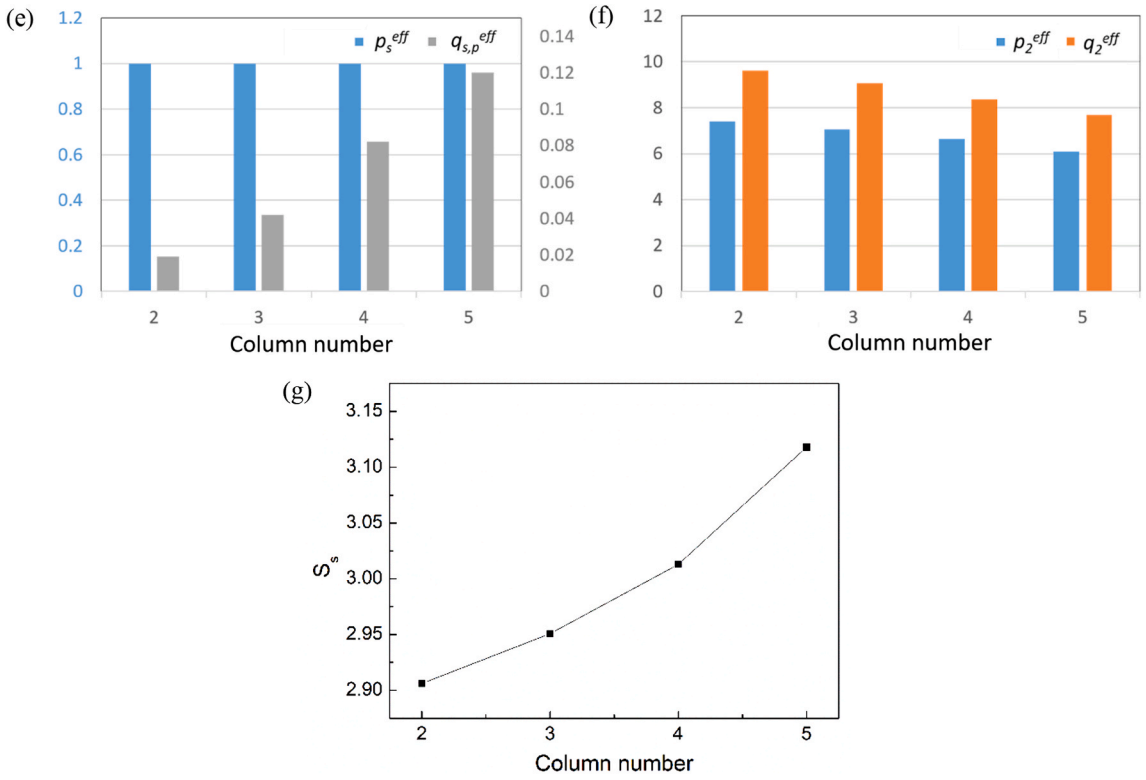

Fig. 5. (*continued*).

gradient increased for larger numbers of columns per unit cell, leading to a lower specific capacity, as shown in Fig. 5c. When the number of columns per cell number exceeded 4, the current density became too large for the electrode to reach a uniform distribution of lithium ion in the electrolyte as a result of limited ion conductivity. The efficiency of material utilization was reduced, leading to a low specific capacity, which further decreased the total capacity and areal capacity (Fig. 5d). The effect of number of columns on characteristic transport properties mirrors that of the number of columns, namely, the electron transport in the solid phase was improved and species transport in electrolyte was reduced (Fig. 5e, f, and g).

4.3.2. *Inverse sphere-structured electrodes*

The unit cell of the inverse sphere structure was constructed by subtracting a sphere from a cube, forming a bottleneck formed at the half-height of the unit cell. The effect of the bottleneck width was studied by changing the radius of the subtracted sphere, as shown in Fig. 6a. It can be observed that the maximum SOC was located at both the bottom and top in the sample with a bottleneck width of 1 w (5.96 μm) (1st figure on the left) and at the top only for bottleneck widths of 5/3 w (9.43 μm), 7/3 w (13.21 μm), and 3 w (16.98 μm) (2nd, 3rd, and 4th figure from left to right), indicating that the bottleneck was switching from electron transport limit in the solid phase to lithium ion diffusion limit in electrolyte. This result was consistent with those observed for the X-structure and the cubic-structure. However, because in inverse sphere structures the competing effects of specific capacity and total mass are much more evident, their areal capacity does not always increase with bottleneck width. The structure with a bottleneck size of 13.21 μm exhibited lower areal capacity than the structure with a 9.43 μm bottleneck (Fig. 6b). As shown in Fig. 6e, f, and g, with increasing bottleneck width, electron transport in the solid phase was promoted significantly, while liquid phase diffusivity and conductivity were reduced.

These results showed that inverse sphere structures affected charge transport to a higher degree than the other two structures. This effect was further demonstrated when the number of columns in sphere-structures was investigated. As shown in Fig. 7b, the solid phase potential decreased from ~0.05 V to ~0.02 V as the number of columns increased, while it was almost constant in cubic-structures (approx. 0.009 V), and exhibited only slight changes in the X-structure (from ~0.014 V to ~0.012 V). Because the bottleneck significantly restricts charge transport, the benefit of an increased bottleneck width is evident. This larger change in solid phase potential had a major effect on SOC distribution; in structures with 2 and 3 columns, the solid phase potential was the main barrier to a uniform distribution. Because the solid phase potential decreased with increasing number of columns, the SOC gradient also decreased from N = 2 to N = 3. Consequently, the maximum specific capacity was achieved for N = 3 (Fig. 7d). Areal capacity was decreased with increased tap density in structures with higher numbers of columns and reached its maximum at N = 4. The effect of the number of columns on species transport was not as significant as that of bottleneck width; however, the effects of bottleneck width and number of columns on species transport were similar (Fig. 7e, f and g).

4.4. *Porosity and electrode thickness*

Two additional controllable parameters in electrode manufacture are thickness and porosity of the electrodes. The overall electrode thickness can be tailored by controlling the amount of electrode material dispensed during 3D printing. The porosity of the 3D electrodes [21] has a two-level hierarchical structure (i.e. micro and macro-scale porosity).

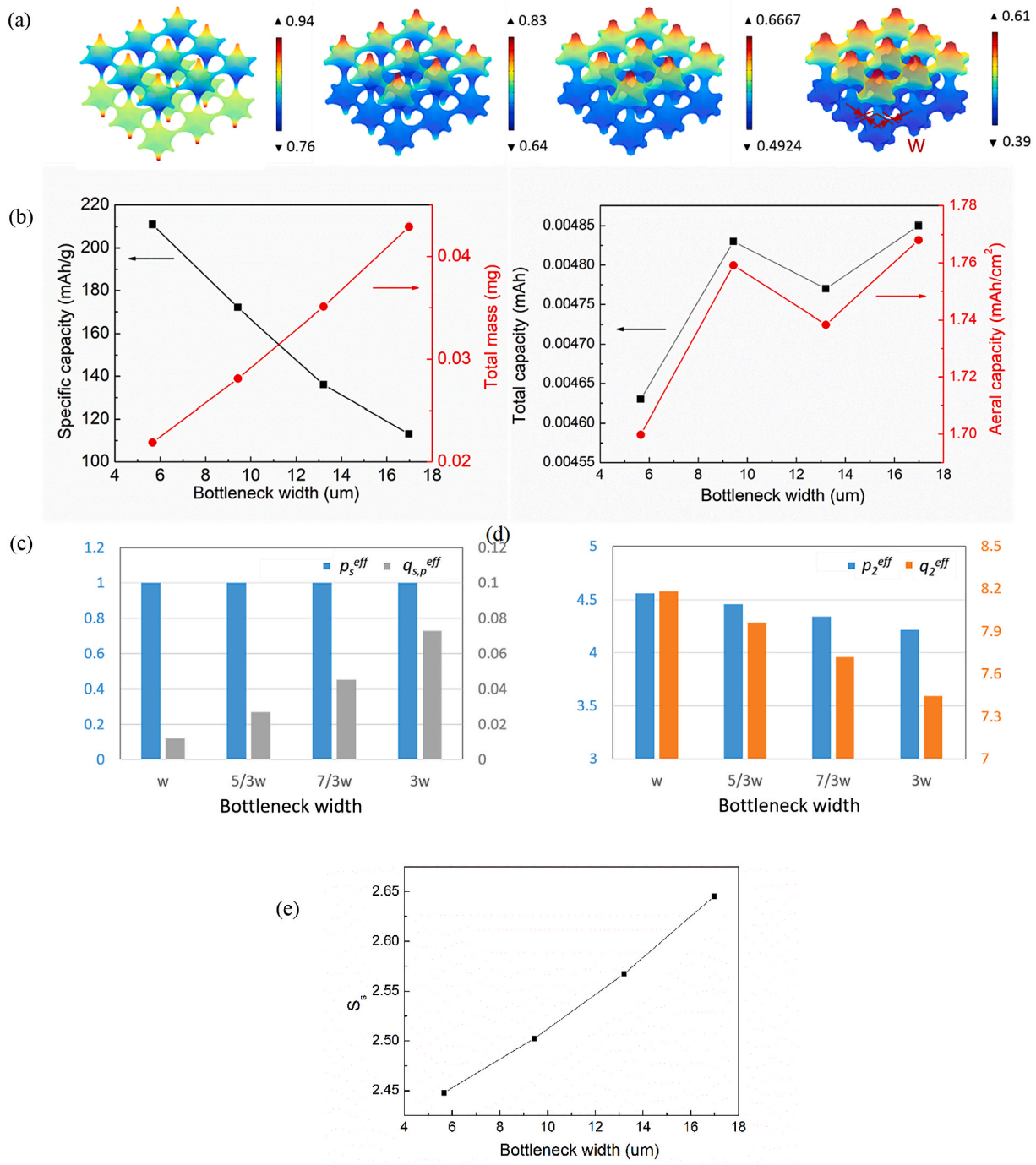

Fig. 6. Effect of bottleneck width in inverse sphere structures. (a) Schematic of inverse sphere structure with different bottleneck widths, (b) Specific capacity, total mass, total capacity, and areal capacity, (c,d) p_s^{eff}, q_s^{eff}, p_2^{eff}, q_2^{eff}, and (e) S_s as functions of bottleneck width in inverse sphere structures.

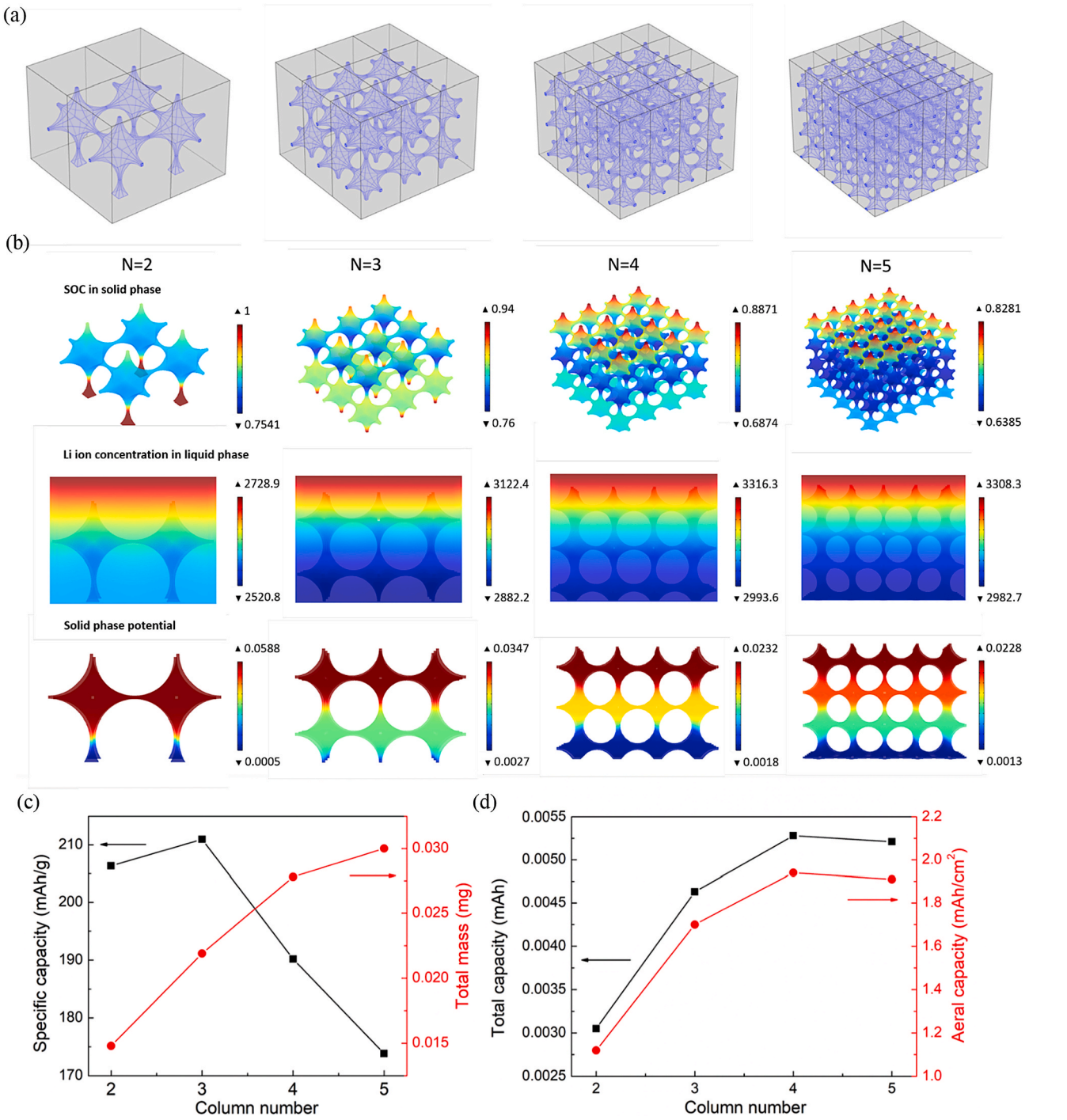

Fig. 7. Effect of number of columns in inverse sphere structures. (a) Schematic of inverse sphere structures with different numbers of columns per unit length, (b) distribution of SOC, electrolyte concentration, and solid phase potential at the end of the discharge in sphere structures with different numbers of columns, (c) specific capacity and total mass, (d) total capacity and areal capacity (e, f, g) p_s^{eff}, q_s^{eff}, p_2^{eff}, q_2^{eff} and S_s as functions of number of columns.

The macro-scale porosity points to the spaces between truss members of the 3D structure, which is in the tens of micrometers. It is treated as a pure electrolyte phase. The micro-level pore structure is the internal porosity within the truss members and is determined by the sintering conditions and is of the order of 1 μm or less. The porosity used this section refer to the internal porosity within the truss members. Fig. 8 shows the specific capacity and areal capacity of the three investigated structures with different thicknesses and levels of porosity.

Fig. 8a, b, and c show that the specific capacity of all the structures decreased as the thickness and solid phase volume fraction (VF) increased. This was attributed to the fact that thicker and denser structures will limit the transport of lithium ions in the electrolyte. However, a thicker and denser structure also means more active material per unit area – in other words, a larger total electrode mass. Fig. 8d, e, and 8f show that the changes in areal capacity are different with increasing electrode thickness and solid phase volume fraction for the three different structures. In a low solid phase volume fraction (VF = 0.2), the effect of thickness was negligible because the large volume

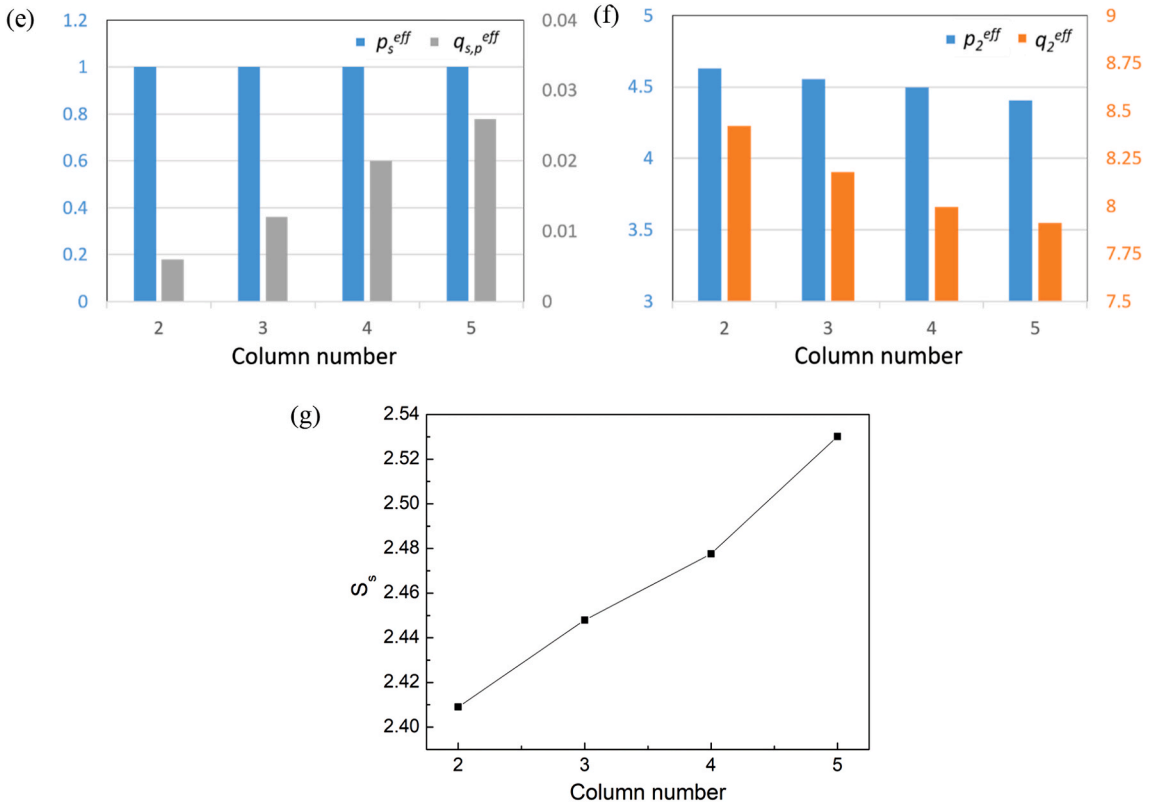

Fig. 7. (*continued*).

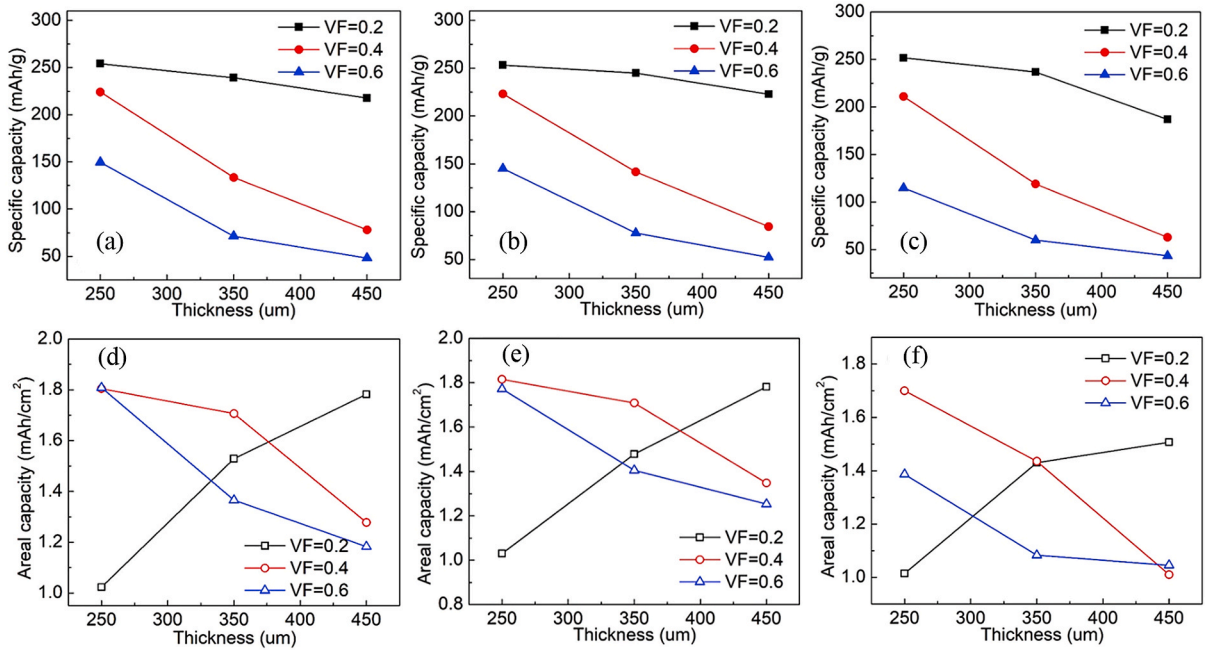

Fig. 8. Effect of thickness and solid phase volume fraction (VF): specific capacity (0.5 C) of (a) X-, (b) cubic-, (c) inverse sphere-structured electrodes as a function of thickness and solid phase volume fraction (VF); areal capacity of (d) X-, (e) cubic-, (f) sphere-structured electrodes as a function of thickness and solid phase volume fraction.

fraction of the electrolyte allowed sufficient diffusion of Li ions. In a high solid phase volume fraction (VF = 0.6), increasing thickness caused inefficient diffusion, leading to a decrease in both specific capacity and areal capacity. According to the simulation results shown in Fig. 8, the optimal parameters to obtain both high specific energy and high areal capacity, X-structure electrodes should have a thickness of 450 μm and VF = 0.2, cubic-structure electrodes should have a thickness of 250 μm and VF = 0.4, and sphere-structure electrodes should have a thickness of 250 μm and VF = 0.4.

5. Conclusions

We carried out an exhaustive study of the effect of 3-dimensional (3D) electrode architectures on the electrochemical performance of batteries and used the gained knowledge to determine optimized electrode structures (anodes and cathodes) for maximum areal and specific capacity. A 3-dimensional full-order electrochemical model, validated by Aerosol Jet printed open octahedral micro-lattice 3D electrodes with a two-level porosity, was used for this analysis. The impact of the electrode geometry was studied by comparing the electrochemical response of electrodes with block-, X-, cubic-structure, and a structure formed by subtracting spheres from a solid block (called 'sphere-structure'). The study revealed that:

i) The primary reason for the superior performance of batteries with 3D electrode architectures is the fact that 3D structures facilitate species transport in the liquid phase. In addition, the main factors affecting battery performance are ion diffusion in the electrolyte and electron transport in the 3D electrode skeleton.
ii) In 3D electrode architectures, the competition between available volume for intercalation and an easier diffusion path for ion and electron transport determines areal/total and specific capacity. Because of this competition, the maximum benefits of a 3D architecture are realized when the length of the structures' truss members is of the order of the diffusion length for the ions in the electrode (~15–20 μm in the current study). In structures with truss members smaller than this scale, the total/areal capacity is too low and discharge rates are too high (undesirable for a battery). At larger length scales, the specific capacity is too low as a result of the increasing difficulty for ion transport through the liquid.
iv) Of the structures studied here, the X- and cubic-structured electrodes demonstrated a larger capacity (35% higher at 0.5C) than the inverse sphere-structured electrodes as a result of more efficient electron transport enabled specifically by the change in electrode geometry. The optimized parameters for these structures for a compromised high specific energy and high areal capacity were a thickness of 450 μm and a volume fraction (VF) of 0.2, a thickness of 250 μm and VF of 0.4, and a thickness of 250 μm and VF of 0.4 for the X-structure, cubic-structure, and sphere-structured electrodes.
iv) If the electrode porosity is reduced, an insufficient diffusion of Li ions in the electrolyte causes a decrease in the electrode capacity even if the electrode volume increases. This was seen in cubic- and X-structured electrodes, where the specific capacity of 3D electrodes decreased with increasing column width and number (columns per unit length). This effect, however, becomes secondary when a bottleneck width emerges in the electrode structure which can impede electron transport through the electrode.
v) The requirement that the length scale of the truss members of optimum 3D architectures be of the order of tens of micrometers limits the availability of manufacturing methods to techniques such as aerosol jet, extrusion, or inkjet 3D printing.

CRediT authorship contribution statement

Yaqi Zhu: Writing - original draft. **Jie Li:** Writing - review & editing. **M. Sadeq Saleh:** Writing - review & editing. **Hiep Pham:** Writing - review & editing. **Rahul Panat:**Conceptualization, Writing - review & editing. **Jonghyun Park:** Conceptualization, Methodology, Writing - review & editing. **Tazdik Patwary Plateau:** Validation.

Declaration of competing interest

The authors declare that they have no known competing financial interests or personal relationships that could have appeared to influence the work reported in this paper.

Acknowledgment

This material is based upon work supported by the National Science Foundation under Grant Nos. CMMI-1563029 and CMMI-1747608.

Appendix A. Supplementary data

Supplementary data to this article can be found online at https://doi.org/10.1016/j.jpowsour.2020.228593.

References

[1] A.K. Padhi, K.S. Nanjundaswamy, J.B. Goodenough, Phospho-olivines as positive-electrode materials for rechargeable lithium batteries, J. Electrochem. Soc. 144 (4) (1997) 1188–1194.
[2] J. Goodenough, A. Manthiram, B. Wnetrzewski, Electrodes for lithium batteries, J. Power Sources 43 (1–3) (1993) 269–275.
[3] J. Hu, et al., 3D-printed cathodes of LiMn1− xFexPO4 nanocrystals achieve both ultrahigh rate and high capacity for advanced lithium-ion battery, Advanced Energy Materials 6 (18) (2016) 1600856.
[4] T.S. Wei, et al., 3D printing of customized li-ion batteries with thick electrodes, Adv. Mater. 30 (16) (2018) 1703027.
[5] L. Chen, et al., 3D printing of artificial leaf with tunable hierarchical porosity for CO2 photoreduction, Chem. Mater. 30 (3) (2018) 799–806.
[6] J.W. Long, et al., Three-dimensional battery architectures, Chem. Rev. 104 (10) (2004) 4463–4492.
[7] K. Sun, et al., 3D printing of interdigitated Li-Ion microbattery architectures, Adv. Mater. 25 (33) (2013) 4539–4543.
[8] K. Fu, et al., Graphene oxide-based electrode inks for 3D-printed lithium-ion batteries, Adv. Mater. 28 (13) (2016) 2587–2594.
[9] J. Li, et al., A hybrid three-dimensionally structured electrode for lithium-ion batteries via 3D printing, Mater. Des. 119 (2017) 417–424.
[10] V.G. Rocha, et al., Multimaterial 3D printing of graphene-based electrodes for electrochemical energy storage using thermoresponsive inks, ACS Appl. Mater. Interfaces 9 (42) (2017) 37136–37145.
[11] D. Cao, et al., 3D printed high-performance lithium metal microbatteries enabled by nanocellulose, Adv. Mater. 31 (14) (2019) 1807313.
[12] C. Liu, et al., Fabrication and characterization of 3D-printed highly-porous 3D LiFePO4 electrodes by low temperature direct writing process, Materials 10 (8) (2017) 934.
[13] C. Liu, et al., High mass loading ultrathick porous Li4Ti5O12 electrodes with improved areal capacity fabricated via low temperature direct writing, Electrochim. Acta 314 (2019) 81–88.
[14] C. Liu, et al., Comparative study on the electrochemical performance of LiFePO4 cathodes fabricated by low temperature 3D printing, direct ink writing and conventional roller coating process, Ceram. Int. 45 (11) (2019) 14188–14197.
[15] B. Yan, et al., Three dimensional simulation of galvanostatic discharge of LiCoO2 cathode based on X-ray nano-CT images, J. Electrochem. Soc. 159 (10) (2012) A1604–A1614.
[16] D.H. Kim, et al., Epidermal electronics, Science 333 (6044) (2011) 838–843.
[17] J.H. Pikul, et al., High-power lithium ion microbatteries from interdigitated three-dimensional bicontinuous nanoporous electrodes, Nat. Commun. 4 (2013) 1732.
[18] X. Li, et al., Mesoporous silicon sponge as an anti-pulverization structure for high-performance lithium-ion battery anodes, Nat. Commun. 5 (2014).
[19] C. Xu, et al., Three-dimensional Au microlattices as positive electrodes for Li–O2 batteries, ACS Nano 9 (6) (2015) 5876–5883.
[20] T.A. Schaedler, et al., Ultralight metallic microlattices, Science 334 (6058) (2011) 962–965.
[21] M.S. Saleh, et al., 3D printed hierarchically-porous microlattice electrode materials for exceptionally high specific capacity and areal capacity lithium ion batteries, Additive Manufacturing 23 (2018) 70–78.
[22] M.S. Saleh, C. Hu, R. Panat, Three-dimensional microarchitected materials and devices using nanoparticle assembly by pointwise spatial printing, Science Advances 3 (3) (2017), e1601986.
[23] A. Sukeshini, et al., Aerosol jet printing and microstructure of SOFC electrolyte and cathode layers, ECS Transactions 35 (1) (2011) 2151–2160.
[24] C. Goth, S. Putzo, J. Franke, Aerosol Jet printing on rapid prototyping materials for fine pitch electronic applications, in: 2011 IEEE 61st Electronic Components and Technology Conference (ECTC), IEEE, 2011.
[25] X. Huang, et al., Ultrahigh rate capabilities of lithium-ion batteries from 3D ordered hierarchically porous electrodes with entrapped active nanoparticles configuration, Adv. Mater. 26 (8) (2014) 1296–1303.
[26] L. Zhang, et al., High-performance hybrid supercapacitor with 3D hierarchical porous flower-like layered double hydroxide grown on nickel foam as binder-free electrode, J. Power Sources 318 (2016) 76–85.
[27] M. Min, et al., Hydrous RuO2/carbon black nanocomposites with 3D porous structure by novel incipient wetness method for supercapacitors, J. Electrochem. Soc. 153 (2) (2006) A334–A338.

[28] Y. Ren, L.J. Hardwick, P.G. Bruce, Lithium intercalation into mesoporous anatase with an ordered 3D pore structure, Angew. Chem. Int. Ed. 49 (14) (2010) 2570–2574.
[29] A. Vu, Y. Qian, A. Stein, Porous electrode materials for lithium-ion batteries – how to prepare them and what makes them special, Advanced Energy Materials 2 (9) (2012) 1056–1085.
[30] F.-S. Ke, et al., Electroplating synthesis and electrochemical properties of macroporous Sn–Cu alloy electrode for lithium-ion batteries, Electrochim. Acta 52 (24) (2007) 6741–6747.
[31] E.M. Sorensen, et al., Three-Dimensionally ordered macroporous Li4Ti5O12: effect of wall structure on electrochemical properties, Chem. Mater. 18 (2) (2006) 482–489.
[32] K. Saravanan, K. Ananthanarayanan, P. Balaya, Mesoporous TiO2 with high packing density for superior lithium storage, Energy Environ. Sci. 3 (7) (2010) 939–948.
[33] W. Dong, J.S. Sakamoto, B. Dunn, Electrochemical properties of vanadium oxide aerogels, Sci. Technol. Adv. Mater. 4 (1) (2003) 3–11.
[34] D. Wang, et al., Synthesis and Li-ion insertion properties of highly crystalline mesoporous rutile TiO2, Chem. Mater. 20 (10) (2008) 3435–3442.
[35] Y. Ren, et al., Influence of size on the rate of mesoporous electrodes for lithium batteries, J. Am. Chem. Soc. 132 (3) (2009) 996–1004.
[36] H. Liu, et al., Highly ordered mesoporous NiO anode material for lithium ion batteries with an excellent electrochemical performance, J. Mater. Chem. 21 (9) (2011) 3046–3052.
[37] C. Jiang, et al., Preparation and rate capability of Li4Ti5O12 hollow-sphere anode material, J. Power Sources 166 (2) (2007) 514–518.
[38] N. Li, et al., Rate capabilities of nanostructured LiMn2 O 4 electrodes in aqueous electrolyte, J. Electrochem. Soc. 147 (6) (2000) 2044–2049.
[39] S.D. Lacey, et al., Extrusion-based 3D printing of hierarchically porous advanced battery electrodes, Adv. Mater. 30 (12) (2018) 1705651.
[40] X. Li, et al., Mesoporous silicon sponge as an anti-pulverization structure for high-performance lithium-ion battery anodes, Nat. Commun. 5 (2014) 4105.
[41] I.V. Thorat, et al., Quantifying tortuosity in porous Li-ion battery materials, J. Power Sources 188 (2) (2009) 592–600.
[42] G.B. Less, et al., Micro-scale modeling of Li-ion batteries: parameterization and validation, J. Electrochem. Soc. 159 (6) (2012) A697–A704.
[43] C.-W. Wang, A.M. Sastry, Mesoscale modeling of a Li-ion polymer cell, J. Electrochem. Soc. 154 (11) (2007) A1035–A1047.
[44] J. Li, et al., Enhanced battery performance through three-dimensional structured electrodes: experimental and modeling study, J. Electrochem. Soc. 165 (14) (2018) A3566–A3573.
[45] D. Wang, et al., Cracking causing cyclic instability of LiFePO4 cathode material, J. Power Sources 140 (1) (2005) 125–128.
[46] S. Bhattacharya, A.R. Riahi, A.T. Alpas, A transmission electron microscopy study of crack formation and propagation in electrochemically cycled graphite electrode in lithium-ion cells, J. Power Sources 196 (20) (2011) 8719–8727.
[47] H. Wang, et al., TEM study of electrochemical cycling-induced damage and disorder in LiCoO2 cathodes for rechargeable lithium batteries, J. Electrochem. Soc. 146 (2) (1999) 473–480.
[48] F. Yang, Interaction between diffusion and chemical stresses, Mater. Sci. Eng. 409 (1–2) (2005) 153–159.
[49] X. Zhang, W. Shyy, A.M. Sastry, Numerical simulation of intercalation-induced stress in Li-ion battery electrode particles, J. Electrochem. Soc. 154 (10) (2007) A910–A916.
[50] M.W. Verbrugge, Y.-T. Cheng, Stress and strain-energy distributions within diffusion-controlled insertion-electrode particles subjected to periodic potential excitations, J. Electrochem. Soc. 156 (11) (2009) A927–A937.
[51] S. Renganathan, et al., Theoretical analysis of stresses in a lithium ion cell, J. Electrochem. Soc. 157 (2) (2010) A155–A163.
[52] X.-G. Yang, C. Bauer, C.-Y. Wang, Sinusoidal current and stress evolutions in lithium-ion batteries, J. Power Sources 327 (2016) 414–422.
[53] R. Fu, M. Xiao, S.-Y. Choe, Modeling, validation and analysis of mechanical stress generation and dimension changes of a pouch type high power Li-ion battery, J. Power Sources 224 (2013) 211–224.
[54] K.-Y. Oh, et al., A novel phenomenological multi-physics model of Li-ion battery cells, J. Power Sources 326 (2016) 447–458.
[55] D. Sauerteig, et al., Electrochemical-mechanical coupled modeling and parameterization of swelling and ionic transport in lithium-ion batteries, J. Power Sources 378 (2018) 235–247.
[56] S. Golmon, K. Maute, M.L. Dunn, Numerical modeling of electrochemical–mechanical interactions in lithium polymer batteries, Comput. Struct. 87 (23–24) (2009) 1567–1579.
[57] J. Newman, W. Tiedemann, Porous-electrode theory with battery applications, AIChE J. 21 (1) (1975) 25–41.
[58] V.R. Subramanian, V.D. Diwakar, D. Tapriyal, Efficient macro-micro scale coupled modeling of batteries, J. Electrochem. Soc. 152 (10) (2005) A2002–A2008.
[59] S. Ashraf, J. Phirani, Capillary displacement of viscous liquids in a multi-layered porous medium, Soft Matter 15 (9) (2019) 2057–2070.
[60] K.C. Kolan, et al., Effect of architecture and porosity on mechanical properties of borate glass scaffolds made by selective laser sintering, in: Proceedings of the 24th Annual International Solid Freeform Fabrication Symposium, 2013 (Austin).